

GALAXY PROPERTIES AND UV ESCAPE FRACTIONS DURING EPOCH OF REIONIZATION: RESULTS FROM THE RENAISSANCE SIMULATIONS

HAO XU¹, JOHN H. WISE², MICHAEL L. NORMAN¹, KYUNGJIN AHN³ AND BRIAN W. O’ SHEA⁴

Draft version April 21, 2022

ABSTRACT

Cosmic reionization is thought to be primarily fueled by the first generations of galaxies. We examine their stellar and gaseous properties, focusing on the star formation rates and the escape of ionizing photons, as a function of halo mass, redshift, and environment using the full suite of the *Renaissance Simulations* with an eye to provide better inputs to global reionization simulations. This suite, carried out with the adaptive mesh refinement code Enzo, is unprecedented in terms of their size and physical ingredients. The simulations probe overdense, average, and underdense regions of the universe of several hundred comoving Mpc³, each yielding a sample of over 3,000 halos in the mass range $10^7 - 10^{9.5} M_{\odot}$ at their final redshifts of 15, 12.5, and 8, respectively. In the process, we simulate the effects of radiative and supernova feedback from 5,000 to 10,000 metal-free (Population III) stars in each simulation. We find that halos as small as $10^7 M_{\odot}$ are able to form stars due to metal-line cooling from earlier enrichment by massive Population III stars. However, we find such halos do not form stars continuously. Using our large sample, we find that the galaxy-halo occupation fraction drops from unity at virial masses above $10^{8.5} M_{\odot}$ to $\sim 50\%$ at $10^8 M_{\odot}$ and $\sim 10\%$ at $10^7 M_{\odot}$, quite independent of redshift and region. Their average ionizing escape fraction is $\sim 5\%$ in the mass range $10^8 - 10^9 M_{\odot}$ and increases with decreasing halo mass below this range, reaching 40–60% at $10^7 M_{\odot}$. Interestingly, we find that the escape fraction varies between 10–20% in halos with virial masses $\sim 3 \times 10^9 M_{\odot}$. Taken together, our results confirm the importance of the smallest galaxies as sources of ionizing radiation contributing to the reionization of the universe.

Subject headings: methods: numerical – radiative transfer – galaxies: high-redshift – galaxies: formation – dark ages, reionization, first stars

1. INTRODUCTION

It is believed that low-mass galaxies at $z \gtrsim 6$ are the primary sources of hydrogen ionizing photons to complete reionization. These galaxies naturally have low signal-to-noise ratios with current telescopes because they are distant and intrinsically dim. Nevertheless, recent observational campaigns have provided valuable constraints on the nature of the first galaxies and their role during reionization. The Hubble Ultra Deep Field (HUDF) 2009 and 2012 campaigns (Ellis et al. 2013) can probe galaxies with rest frame UV magnitude as low as ~ -18 at $z \gtrsim 7$ and as distant as $z \simeq 11$ (McLure et al. 2011; Zheng et al. 2012; Coe et al. 2013; Finkelstein et al. 2015; Oesch et al. 2016).

It is clear that UV ionizing photons from these observed “bright galaxies” are not enough to fully ionize the universe by $z = 6$ (Robertson et al. 2013), as implied by quasar observations (Fan et al. 2006), thus fainter galaxies and other ionizing sources (e.g. accreting black holes) are needed to provide the remaining ionizing photons. Robertson et al. (2015), by extrapolating the UV luminosity function (LF) with a steep faint end slope < -2 (e.g. Bouwens et al. 2011, 2015; McLure et al.

2013), have shown that the LF must extend to $M_{UV} \sim -13$ to be consistent with the integrated Thomson optical depth $\tau_{es} = 0.066 \pm 0.012$ measured by the *Planck* satellite (Planck Collaboration et al. 2015). Galaxies with such magnitudes have stellar masses as small as $10^6 M_{\odot}$ in halos with masses $M \sim 10^8 M_{\odot}$, providing sufficient UV radiation to complete and maintain reionization. Furthermore, the uncertainty in τ_{es} allows for some contribution from star formation occurring in minihalos with masses $M \lesssim 10^8 M_{\odot}$ (Ahn et al. 2012; Salvadori et al. 2014).

This unseen population of even fainter and, perhaps, more abundant galaxies will eventually be detected by next-generation telescopes such the *James Webb Space Telescope* (JWST, launch date 2018; Gardner et al. 2006) and 30-meter class ground-based telescopes⁵. However, the growth of these small galaxies can be complicated by feedback from both metal-free (Population III; Pop III) and metal-enriched stars, where H II regions and supernovae (SNe) can drive outflows larger than the escape velocity of their host halo (Whalen et al. 2004, 2008; Kitayama et al. 2004; Kitayama & Yoshida 2005; Abel et al. 2007), leaving behind a gas-poor halo that only recovers by cosmological accretion after tens of Myr (Wise & Abel 2008b; Greif et al. 2010; Wise et al. 2012b; Muratov et al. 2013; Jeon et al. 2014). On the other hand, these SNe also pre-enrich the gas that ultimately assembles the first galaxies to $10^{-4} - 10^{-3} Z_{\odot}$ (Bromm et al. 2003; Wise & Abel 2008b; Karlsson et al. 2008; Greif et al. 2010; Wise

¹ Center for Astrophysics and Space Sciences, and San Diego Supercomputer Center, University of California, San Diego, 9500 Gilman Drive, La Jolla, CA 92093; hxu@ucsd.edu, mlnorman@ucsd.edu

² Center for Relativistic Astrophysics, School of Physics, Georgia Institute of Technology, 837 State Street, Atlanta, GA 30332; jwise@gatech.edu

³ Department of Earth Science Education, Chosun University, Gwangju 501-759, Korea; kjahn@chosun.ac.kr

⁴ Department of Computational Mathematics, Science and Engineering, Department of Physics and Astronomy, and National Superconducting Cyclotron Laboratory, Michigan State University, East Lansing, MI 48824; oshea@msu.edu

⁵ European Extremely Large Telescope (E-ELT, 39-m, completion date 2024; Gilmozzi & Spyromilio 2007), Giant Magellan Telescope (GMT, 24.5-m, completion date 2020; Johns et al. 2012), Thirty Meter Telescope (TMT, 30-m, completion date 2022; Simard 2013)

et al. 2012b). Prior to cosmological reionization, galaxies can then form in DM halos as small as $10^7 M_\odot$. Low-mass ($V_c = \sqrt{GM_{\text{vir}}/R_{\text{vir}}} \lesssim 30 \text{ km s}^{-1}$) galaxies may provide $\sim 40\%$ of the ionizing photons to reionization, eventually becoming photo-suppressed as reionization ensues (Wise et al. 2014). A small fraction (5–15%) of these first galaxies may survive until the present day (Gnedin & Kravtsov 2006), and ultra-faint dwarf galaxies (UFDs) discovered in the Sloan Digital Sky Survey (SDSS) that surround the Milky Way could be the fossils of this subset of the first galaxies, providing a way to estimate the abundance of dwarf galaxies during the epoch of reionization (Bullock et al. 2000; Salvadori & Ferrara 2009; Bovill & Ricotti 2011; Weisz et al. 2014; Boylan-Kolchin et al. 2014; Wheeler et al. 2015).

Provided that there is sufficient star formation during reionization, the next question is the fraction of ionizing photons, f_{esc} , that can escape their host halos into the intergalactic medium (IGM). This quantity is difficult to measure both observationally and theoretically. It is nearly impossible to detect Lyman continuum (LyC) emission at $z > 4$ because Lyman limit systems become much more abundant with increasing redshift (Inoue & Iwata 2008). Detecting LyC emission only becomes feasible at $z \sim 3$ when the IGM optical depth is around unity. Deep narrow-band galaxy spectroscopy and imaging have detected LyC emission in numerous $z \sim 3$ galaxies with f_{esc} values ranging from an upper limit of 7–9% for bright galaxies (Siana et al. 2015) to 10–30% for fainter Lyman- α emitters (Nestor et al. 2013) and $33 \pm 7\%$ for “Lyman-continuum galaxies” (Cooke et al. 2014). However, these observations are susceptible to foreground contamination from lower redshift galaxies in the same line of sight (e.g. Vanzella et al. 2012; Siana et al. 2015; Grazian et al. 2016).

Simulations have suggested that the escape fraction is on the order of a few percent for halos with masses $\geq 10^{11} M_\odot$ (Dove et al. 2000; Razoumov & Sommer-Larsen 2007; Gnedin 2008; Yajima et al. 2011). Conversely, recent post-processing results from the EAGLE simulation (Schaye et al. 2015) estimated that f_{esc} is on the order 10–20% in galaxies with star formation rates $\text{SFR} \geq 1 M_\odot \text{ yr}^{-1}$ and increases with SFR (Sharma et al. 2016). By redshift 6, they found that galaxies with $M_{\text{UV}} < -18$ may provide half of the photon budget to the global ionizing emissivity. If lower-mass galaxies have similar escape fractions before reionization, there are not enough ionizing photons that can escape galaxies to reionize the universe by $z = 6$ (Gnedin 2008).

The escape fraction from small galaxies is also under debate. Wood & Loeb (2000) argued that $f_{\text{esc}} \leq 0.01$, due to the higher mean densities at high redshifts. Using idealized isolated galaxy calculations, Fujita et al. (2003) found that $f_{\text{esc}} \leq 0.01$ from dwarf starburst disc galaxies with total masses between 10^8 and $10^{10} M_\odot$, and Paardekooper et al. (2011) found similar results for high-redshift disc galaxies with total masses of 10^8 and $10^9 M_\odot$. In contrast, Ricotti & Shull (2000) found higher escape fraction $f_{\text{esc}} \geq 0.1$ in high-redshift halos with masses $M \leq 10^7 M_\odot$. Such escape fraction values were then further confirmed by several numerical simulations (Wise & Cen 2009; Razoumov & Sommer-Larsen 2010; Yajima et al. 2011; Paardekooper et al. 2013, 2015; Ferrara & Loeb 2013). Wise et al. (2014), using high resolution cosmological radiation hydrodynamics simulations of early galaxies, showed that the mean escape fraction of hydrogen ionizing photons decreases with increasing halo mass. They found that the amount of ionizing photons per unit mass

escaping from a halo exhibits little evolution with a wide halo mass range, from $10^{6.75}$ to $10^{8.75} M_\odot$. They concluded that low-mass galaxies ($M_{\text{halo}} \geq 10^8 M_\odot$) may produce a significant amount of the ionizing photons escaping into the IGM at $z \geq 10$ during cosmic reionization, suggesting that the faintest galaxies ($M_{\text{UV}} \geq -12$) are very important in the early stage of the epoch of reionization.

However, star formation in these low-mass galaxies is suppressed as reionization progresses, and galaxies that are not susceptible to photo-evaporation ($M_{\text{vir}} \gtrsim 10^9 M_\odot$) provide the remaining ionizing radiation to complete reionization. Post-process radiative transfer calculations (Ma et al. 2015; Sharma et al. 2016) and radiation hydrodynamics simulations (Kimm & Cen 2014; Gnedin 2016) that studied this mass range found that f_{esc} is highly variable in a single galaxy and has a large scatter for a given galaxy mass, halo mass, or UV luminosity. Time-averaged f_{esc} values between 3–15% in halos with $M_{\text{vir}} \gtrsim 10^9 M_\odot$, but any trends with halo mass or redshift either weak or inconsistent between groups. Further complicating the issue, runaway and binary stars may boost f_{esc} values by a few percent (Conroy & Kratter 2012; Kimm & Cen 2014; Ma et al. 2016).

A major caveat in the work of Wise et al. is that the simulation volume of 1 comoving Mpc^3 is small and has no large-scale variance in cosmological density distribution. There are only 32 dwarf galaxies at the final redshift, and the simulation does not capture galaxies forming in halos more massive than $10^9 M_\odot$. So, in their paper they combined the data at different redshifts to statistically evaluate the galaxy properties of star formation and escape fraction by assuming that these properties are independent of redshift and environment.

In this work, we characterize the abundance and escape fraction of ionizing radiation from faint galaxies before cosmic reionization utilizing a suite of zoom-in cosmological radiation hydrodynamics simulations, named the *Renaissance Simulations*, that survey three regions with varying large-scale overdensities. These quantities are extremely important in understanding the progression of reionization. Each simulation in this work improves the statistics of the first galaxy properties in Wise et al. (2014) by a factor of ~ 100 . We validate their scheme to combine data from different times, confirm their results in different environments, and extend the analysis to slightly more massive galaxies. In addition to elucidating the ionizing photon budget during cosmic reionization, our work can provide valuable constraints on the process of reionization. We first describe our simulation setup in Section 2. Then, in Section 3, we present results on the overall baryonic galaxy properties, on how reionization initially proceeds, and on the similarity of galaxy properties in different large-scale environments. We then describe the method used to calculate ionizing escape fractions in each galaxy and present the variations of this fraction in Section 4. Last, we discuss and conclude our findings in Section 5.

2. SIMULATIONS

We present results from the *Renaissance Simulations*, a suite of zoom-in calculations that focus on high-redshift ($z \geq 8$) galaxy formation and the ensuing reionization, which were originally presented in O’Shea et al. (2015). Each simulation encompasses a different large-scale environment with a comoving volume of $\sim 200 \text{ Mpc}^3$ and includes metal-free and metal-enriched star formation and feedback. These simulations self-consistently capture the formation of nearly 3,000

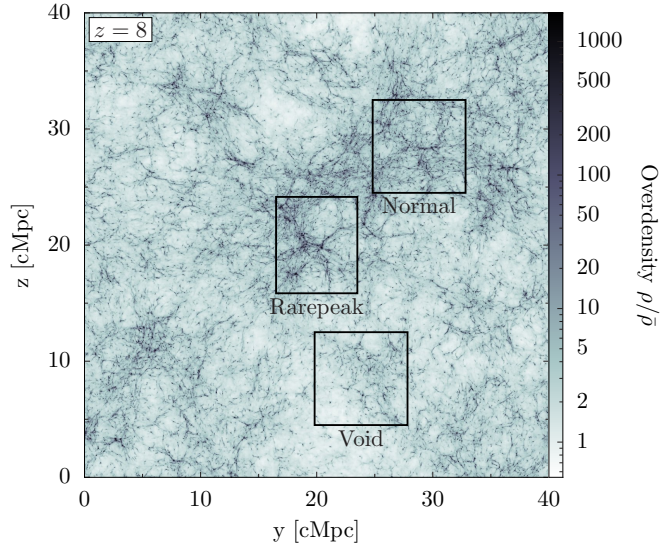


Figure 1. Mass-weighted density projection of the (40 comoving Mpc)³ exploratory dark matter simulation at $z = 8$. The survey volumes of the Rarepeak, Normal, and Void regions are outlined. The Rarepeak region is centered on the most massive halo at $z = 6$. Due to projection effects, the normal region appears as dense as the Rarepeak, however its average overdensity is only 9% higher than the mean matter density.

of the first generations of galaxies, and we study their surrounding environment, their baryonic properties, and the self-regulation of their star formation. More specifically, we focus on the photo-ionization and photo-heating of the IGM and the role of the first galaxies during reionization. We have previously presented results from the most overdense region (the “Rare Peak” simulation) in the *Renaissance Simulations* on the Pop III stellar distribution (Xu et al. 2013), X-rays from Pop III binaries (Xu et al. 2014), their 21-cm signal (Ahn et al. 2015), their scaling relations (Chen et al. 2014), and the galaxy luminosity function (O’Shea et al. 2015).

2.1. Simulation setup

We use the adaptive mesh refinement (AMR) cosmological hydrodynamics code *Enzo* (Bryan et al. 2014), along with its adaptive ray tracing module *Enzo+Moray* (Wise & Abel 2011) for the transport of ionizing radiation, which is coupled to the hydrodynamics and chemistry in *Enzo*.

All of the *Renaissance Simulations* are performed in the same comoving volume of (40 Mpc)³. The initial conditions for this volume are generated using MUSIC (Hahn & Abel 2011) with second-order Lagrangian perturbations at $z = 99$ using a 512^3 root grid resolution. We use the cosmological parameters from the 7-year WMAP Λ CDM+SZ+LENS best fit (Komatsu et al. 2011): $\Omega_M = 0.266$, $\Omega_\Lambda = 0.734$, $\Omega_b = 0.0449$, $h = 0.71$, $\sigma_8 = 0.81$, and $n = 0.963$.

It is computationally prohibitive to have the necessary parsec-scale spatial resolution (and accompanying mass resolution), which is required to marginally resolve star forming molecular clouds, throughout the entire simulation volume. We perform zoom-in simulations on three selected regions, ranging from 220 to 430 comoving Mpc³ with different overdensities, providing a mixture of large-scale environments. We first run a 512^3 N-body only simulation to $z = 6$. We then select an overdense region (“Rarepeak”), a nearly mean density region (“Normal”) and an underdense region (“Void”), which are displayed in Figure 1. The selec-

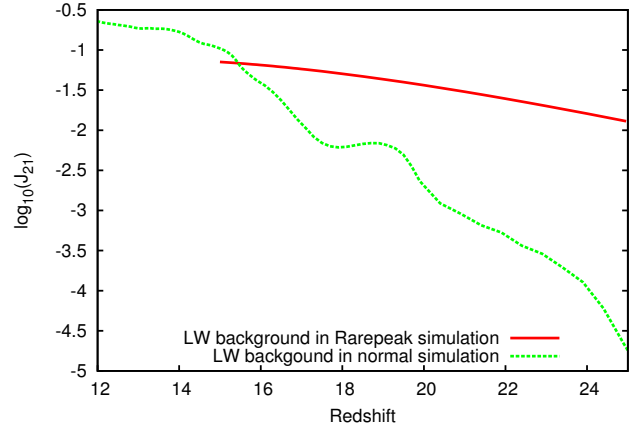


Figure 2. Evolution of the intensity of the LW background used in the Normal (green) and Rarepeak (red) simulations. The intensity in the Rarepeak is calculated with Equation (1) and is higher because it considers the global emissivity from Pop III stars, whereas the self-consistent calculation in the Normal simulation does not.

tion of the survey volume and detailed setup of the Rarepeak have been described in Xu et al. (2013), which is centered on two $3 \times 10^{10} M_\odot$ halos at $z = 6$ with a survey volume of $(3.8 \times 5.4 \times 6.6) \text{ Mpc}^3$. For both the Normal and Void runs, we select comoving volumes of $(6.0 \times 6.0 \times 6.125) \text{ Mpc}^3$ as the survey volumes. We then re-initialize all simulations, having the survey volume at the center, with 3 more static nested grids to have an effective resolution of 4096^3 and an effective dark matter mass resolution of $2.9 \times 10^4 M_\odot$ inside the highest static nested grid that encompasses the survey volume. During the course of the simulation, we allow a maximum refinement level $l = 12$, resulting in a maximal resolution of 19 comoving pc. The refinement criteria employed are the same as in Wise et al. (2012b), refining on baryon and dark matter overdensities of 4 and local Jeans length by at least 4 cells (Truelove et al. 1998) and is restricted to the survey volumes. While the Rarepeak simulation adjusts the survey volume size during the simulation to contain only the highest resolution dark matter particles of the highest static nested grid, matter in the Normal and Void simulations is not fully contained in a large-scale potential well and have significant peculiar velocities, causing some of the high-resolution particles to migrate out of the initial static grid. Thus, we simplify the simulation setup by restricting grid refinement to occur in the initial high-resolution grid instead of its Lagrangian region. We stop the simulations of the Rarepeak, Normal, and Void regions at $z = (15, 12.5, 8)$, respectively, because of the high computational cost of the radiative transfer. The Renaissance simulations were run on the Blue Waters system at NCSA. Each simulation used approximately eight million core-hours.

2.2. Lyman-Werner Background

All of the simulations use the same chemistry, cooling, metal-free and metal-enriched star formation, and radiative and supernova feedback models, which are fully described in Wise et al. (2012a) and Xu et al. (2013). We model the H₂ dissociating radiation with an optically-thin, inverse square profile, centered on all metal enriched and Pop III star particles. However, while we use the same model for Lyman-Werner (LW) radiation from stellar sources, different LW backgrounds are used in different simulations. LW radiation may significantly delay the Pop III formation in low mass

halos (Machacek et al. 2001; Wise & Abel 2007; O’Shea & Norman 2008), and thus the enrichment history and the emergence of metal-enriched stars in those halos.

The three simulations reported in the paper use three different LW background models. For the Rarepeak simulation, we use the time-dependent LW optically thin radiation background used in Wise et al. (2012b), which is based on the semi-analytical model of Wise & Abel (2005), updated with the 7-year WMAP parameters and optical depth to Thomson scattering. This model considers the LW contributions of Pop III stars and is valid at higher redshifts ($z \gtrsim 12$) before metal-enriched stars dominate the cosmic emissivity. We use the functional form of the background evolution in Wise et al. (2012b),

$$\log_{10} J_{21}(z) = A + Bz + Cz^2 + Dz^3 + Ez^4, \quad (1)$$

where $(A, B, C, D, E) = (-2.567, 0.4562, -0.02680, 5.882 \times 10^{-4}, -5.056 \times 10^{-6})$, and J_{21} is the specific intensity in units of $10^{-21} \text{ erg s}^{-1} \text{ cm}^{-2} \text{ Hz}^{-1} \text{ sr}^{-1}$. In the high density region of the Rarepeak simulation, the LW radiation from local Pop III and metal-enriched star sources dominate this LW background at redshifts as early as 20.

For the Normal region, we calculate the LW background self-consistently by considering the actual evolution of sources inside the simulation box. This choice is justified by the fact that the Normal region is indeed a good representation of an average patch of the Universe. We assume that sources outside the simulation box are uniformly distributed, which is a good approximation because the spatial fluctuations of the source distribution is smeared out when the sources are located very far from the observing point. Then the background $J_{21}(z)$ is given by the following calculation (Ahn et al. 2009):

$$J_{21}(z) = (1+z)^3 \int_0^{r_{\text{LW}}} \frac{dr_{\text{os}}}{1+z_s} \bar{J}_{\nu_s}(z_s) f_{\text{mod}}(r_{\text{os}}), \quad (2)$$

where $\bar{J}_{\nu_s}(z_s)$ is the band-averaged emission coefficient (in $\text{erg s}^{-1} \text{ Hz}^{-1} \text{ sr}^{-1} \text{ cm}^{-3}$) in the rest-frame photon energy range [11.5, 13.6] eV at the source redshift z_s ,

$$r_{\text{os}} \equiv 2cH_0^{-1} \Omega_m^{-1/2} \left[(1+z_{\text{obs}})^{-1/2} - (1+z_s)^{-1/2} \right] \quad (3)$$

is the comoving distance traveled by a photon from the source to the observing point, and the intensity is modulated by the ‘‘picket-fence modulation factor’’ f_{mod} given by

$$f_{\text{mod}} = \begin{cases} 1.7 \exp \left[- \left(\frac{r_{\text{os}}/\text{Mpc}}{116.29\alpha} \right)^{0.68} \right] - 0.7 & \text{if } r_{\text{os}} \leq 97.39\alpha \text{ Mpc} \\ 0 & \text{otherwise,} \end{cases} \quad (4)$$

where a scaling factor,

$$\alpha = \left(\frac{h}{0.7} \right)^{-1} \left(\frac{\Omega_m}{0.27} \right)^{-0.5} \left(\frac{1+z_s}{21} \right)^{-0.5}, \quad (5)$$

defines the LW horizon $r_{\text{LW}} \equiv 97.39\alpha \text{ Mpc}$, beyond which no sources contribute to J_{LW} . We calculate $\bar{J}_{\nu_s}(z_s)$ by averaging the source luminosity inside the box as

$$\bar{J}_{\nu_s}(z_s) = \frac{1}{4\pi l^3} \sum_i \bar{L}_{\nu_s,i}(z_s), \quad (6)$$

where $\bar{L}_{\nu_s,i} \equiv \int_{11.5 \text{ eV}}^{13.6 \text{ eV}} dE L_{\nu_s,i}/(2.1 \text{ eV})$ is the band-averaged

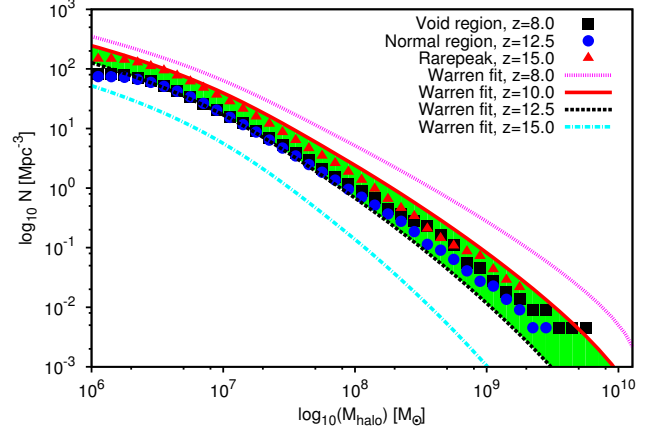


Figure 3. Halo mass function within refined regions from the simulations (points) and the analytic fit (lines) from Warren et al. (2006) at various redshifts. The green shaded area denotes the halo number density from the Warren et al. fit between $z = 12.5$ and $z = 10$, and the simulated halo mass function of all of the regions lie within this range.

luminosity (Schaerer 2002) of source i and l is the (proper) size of the simulation box.

Figure 2 shows the intensity of the LW background used in the simulations of Normal region and Rarepeak in units of J_{21} ($10^{-21} \text{ erg s}^{-1} \text{ cm}^{-2} \text{ Hz}^{-1} \text{ sr}^{-1}$). The background in the Rarepeak simulation is computed with Equation (1) and is higher at early times because it incorporates the emissivity from Pop III stars. The LW background is strong enough to delay the formation of Pop III stars in low mass halos ($< 10^7 M_{\odot}$) (O’Shea & Norman 2008), but will be dominated by local sources with active stars.

The Void simulation runs the fastest because of the small amount of structure formation relative to the other two simulations, and we are able to evolve it down to $z = 8$. From the latest Planck results (Planck Collaboration et al. 2015), the universe is roughly half ionized at this point. Because we use the Normal simulation for the self-consistent LW background, which ends at $z = 12.5$, we do not use a LW background for the Void simulation and only consider LW radiation from internal sources. Thus, we expect higher Pop III star formation rates that occur in smaller halos and an earlier transition to metal-enriched stars. We have re-run the Void simulation with the Wise & Abel (2005) LW background prescription and found that the impact is modest, increasing the total Pop III stellar mass in the simulation by 7% and does not affect the metal-enriched star formation rate density (see Figure 2 in Xu et al. 2016). We will not discuss the detailed effects of the LW background on first galaxy formation and cosmic evolution in this paper, though our simulations have shown that the different LW background has some important impacts on star formations at high redshift and in low mass halos. They do not significantly change the results of this paper on ionizing photon production and their escape fractions.

3. SIMULATED GALAXY PROPERTIES

We focus on the role of the first generations of galaxies in cosmic reionization. We first explore their global properties in the three different regions of the *Renaissance Simulations*. We then calculate the distribution of various baryonic properties of the star-forming halos and the ensuing reionization from this galaxy population. We then describe the UV lumi-

Table 1
Summary of simulations

Region (1)	z (2)	$\delta\rho$ (3)	N_{halo}			N_{III} (7)	$M_{\text{II}} (M_{\odot})$ (8)	N_{ion} (9)	f_{H}	
			$> 10^7 M_{\odot}$ (4)	$> 10^8 M_{\odot}$ (5)	$> 10^9 M_{\odot}$ (6)				vw (10)	mw (11)
Void	8	-0.256	3263	172	5	5110	6.27×10^8	3.87×10^{69}	0.117	0.132
Normal	12.5	0.0927	3275	137	3	6544	1.92×10^8	1.20×10^{69}	0.020	0.030
Rarepeak	15	0.686	3675	174	4	10112	6.09×10^8	2.98×10^{69}	0.056	0.076

Notes: Column (1): Name of simulation. Column (2): Redshift. Column (3): Overdensity of the region. Columns (4) to (6): Number of halos with mass larger than 10^7 , 10^8 , and $10^9 M_{\odot}$, respectively. Column (7): Number of Pop III stars and remnants. Column (8): Metal-enriched stellar mass. Column (9): Total number of ionizing photons generated during the simulation. Columns (10) and (11): Volume-weighted and mass-weighted hydrogen ionization fraction.

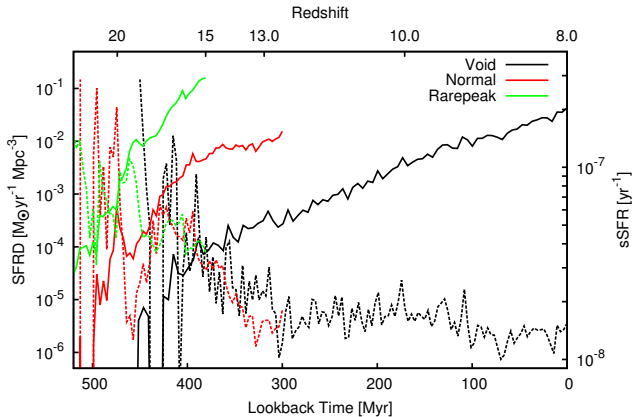


Figure 4. Evolution of star formation rate density (solid lines) and specific star formation rate (dashed lines). The star formation densities increase more rapidly in the more dense regions, as expected.

nosity function of these galaxies and discuss the similarities of our simulated galaxies in different survey volumes at various times.

3.1. Early Galaxy Properties in Different Environments

We first present the global properties of the three survey volumes at the final simulation redshift $z = (15, 12.5, 8)$ for the Rarepeak, Normal, and Void regions, respectively. Table 1 summarizes the overall overdensity, halo counts, Pop III star counts, metal-enriched stellar masses, total number of ionizing photons produced, and ionized fraction. Each simulation has more than 3,000 halos with masses $M > 10^7 M_{\odot}$ that are viable hosts for star formation during the epoch of reionization. Between 5,000 and 10,000 Pop III stars form in each of the regions, leading to over $10^8 M_{\odot}$ of metal-enriched star formation after the initial enrichment. In total, over 10^{69} UV ionizing photons are emitted from these stellar populations that ionize 13%, 3%, and 8% of the mass in the Void, Normal, and Rarepeak volumes at the final redshift.

Before interpreting the results from the simulations, we first check how representative these regions are of a typical patch of the universe. By construction, the Rarepeak, Normal, and Void simulations capture high, mean, and low density regions, respectively. Figure 3 shows the simulated halo mass functions (HMFs) compared to the analytic mass function of Warren et al. (2006), which is calibrated by various N -body simulations and ellipsoidal collapse models of Press-Schechter formalism (Press & Schechter 1974; Sheth & Tormen 1999). All of the HMFs reside between the Warren fits at $z = 12.5$ and 10, depicted by the shaded region in Figure 3. The Normal HMF at $z = 12.5$ fits well with the analytic fit at $z = 12.5$ between 5×10^6 and $10^8 M_{\odot}$, but the volume contains some

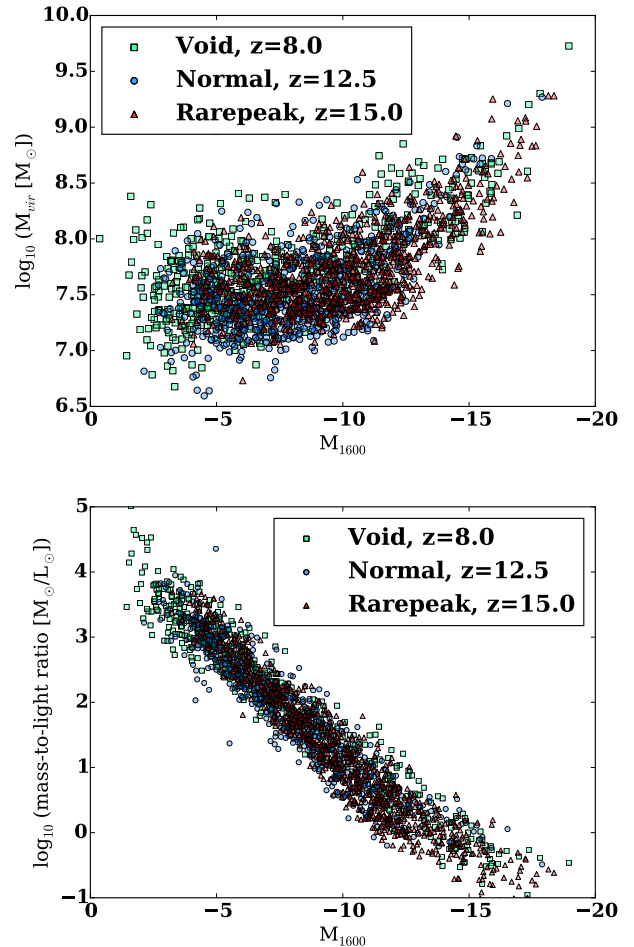


Figure 5. Scatter plots of virial mass (top panel) and mass (virial) to light ratio (bottom panel), in solar units, as functions of UV magnitude for the Void region at $z = 8$ (green squares), the Normal region at $z = 12.5$ (blue circles) and the Rarepeak at $z = 15$ (red triangles), respectively. Each point represents a single galaxy.

small-scale overdense modes, resulting in an overabundance of halos with $M > 10^8 M_{\odot}$. The Rarepeak and Void HMFs have much higher and lower halo number densities than the analytic fit, demonstrating that they truly vary from the cosmic mean. The Void HMF is greater than the Warren fit at $z = 12.5$ in the high-mass end that is caused by a few overdense smaller scale regions, similar to the Normal region.

We show the star formation rate densities (SFRD) and specific star formation rate, ($s\text{SFR} = \text{SFR}/M_*$) for all three regions in Figure 4. In each region, the different large-scale overdensities drive SFRD variations with the Rarepeak

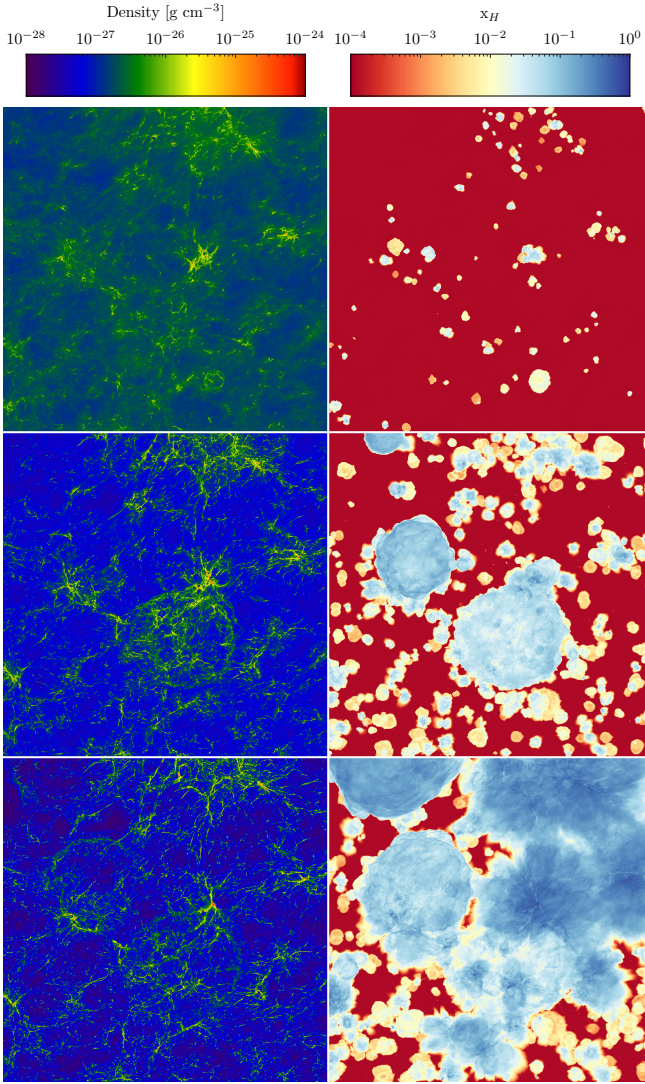


Figure 6. Projections of density-weighted baryon density (left) and hydrogen ionization fraction (right) of the Void region at $z = 15$ (top), 10 (middle) and 8 (bottom). The projected volume is a cube with sides of 6.1 comoving Mpc.

(Void) region forming stars over an order of magnitude higher (lower) than the Normal region at any given time.

The number density of halos and star formation histories of the three simulated regions are quite different. One important question to raise about simulations that probe different environments is whether these galaxies can be considered to be a single population that mainly depends on halo mass without much variation on environmental factors and redshift during the early stages of cosmic reionization. Figure 5 shows the virial mass and mass-to-light ratio as a function of their total AB magnitude at 1600 \AA , M_{1600} . To compute the magnitude, we determine the spectral energy distribution (SED) for each galaxy with the stellar population synthesis model of [Bruzual & Charlot \(2003\)](#). We use the ages, masses, and metallicities of the metal-enriched star particles as input, assuming an instantaneous burst model. We do not consider any nebular emission lines in the SEDs. In galaxies with $M_{1600} \lesssim -12$, brighter galaxies are clearly hosted in larger halos. Dimmer galaxies, however, are hosted in halos with masses ranging from 3×10^6 to $3 \times 10^8 M_{\odot}$. These small and dim galaxies are

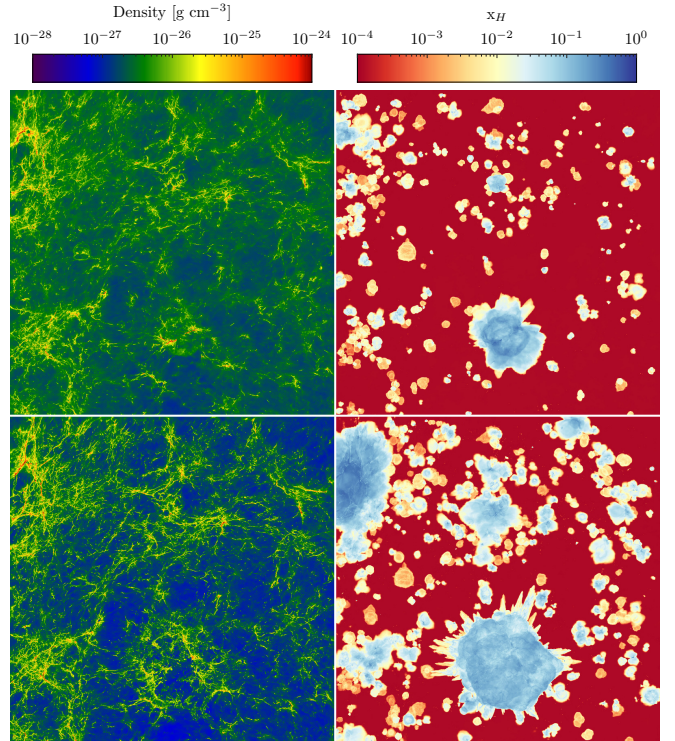


Figure 7. Same as Figure 6 but for the Normal region at $z = 15$ (top) and $z = 12.5$ (bottom).

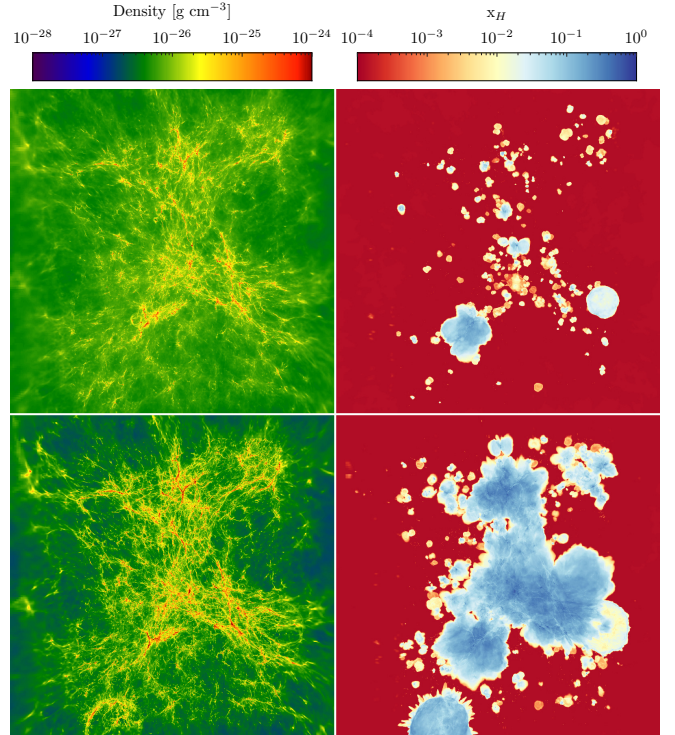


Figure 8. Same as Figure 6 but for the Rarepeak region at $z = 18.5$ (top) and $z = 15$ (bottom).

usually the result of one burst of star formation that has subsequently aged. No new star formation occurred afterwards as the gas supply has been disrupted by supernova and radiative feedback. The mass-to-light ratio shows a more monotonic decreasing trend with increasing luminosity, similar to those

found in local dwarf galaxies (McConnachie 2012). These two trends are apparent in each of the three regions, where the overlap of the data points suggest that they can be considered as a single galaxy population that is independent of large-scale environment and redshift, given that it is before cosmic reionization. Thus, we analyze the three regions as one galaxy sample throughout the rest of the paper. We discuss this simplification further in §3.4 before presenting our results on the UV escape fraction.

3.2. Ionization of the IGM

We show projections of baryon density and hydrogen ionization fraction of the Void, Normal, and Rarepeak regions in Figures 6–8, respectively, that use the same color scales at various redshifts. The differences in the large-scale overdensities are clearly seen in the density projections. The standard reionization picture is apparent in the Void simulation, starting with isolated H II regions at higher redshifts (top row; $z = 15$). These then grow and merge, forming progressively larger volumes at later times, resulting in several \sim cMpc scale H II regions at $z = 8$. In the Void simulation, a significant fraction of the ionizing radiation leaves the survey volume, and they are not considered in the calculation of the ionization fraction. Interestingly, the galaxies in the Rarepeak produce a similar amount of ionizing photons by $z = 15$ as the Void region at $z = 8$ (see Figure 9). The typical H II regions are much smaller, however; this is caused by higher recombination rates, which are proportional to n^2 in ionized regions and thus strongly scale as $(1+z)^6$ that results in a difference of a factor of ~ 30 between the final redshifts of the Rarepeak and Void regions.

Predictably, the ionization history in our three survey volumes differ substantially. Figure 9 shows the ionization fraction, total number of ionizing photons emitted, and the ratio of ionizing photons to hydrogen atoms. The Rarepeak region, as expected, proceeds to form stars and ionize the region at a much faster pace than the other regions. Because the H II regions are small and confined at $z \gtrsim 12$ in all simulations, the mass-weighted ionization fractions are significantly higher than the volume-weighted ones. For all simulations at their ending redshift, the photon-to-baryon ratio is greater than unity, demonstrating that most photons are lost to recombination processes over cosmic time.

3.3. Galaxy properties and UV luminosity function

We now focus on the individual properties of the simulated galaxies in our three survey regions. We plot the distribution of the stellar mass M_* , star formation rate, gas mass fraction $f_{\text{gas}} \equiv M_{\text{gas}}/M_{\text{vir}}$, and stellar baryonic fraction $f_* \equiv M_*/M_{\text{gas}}$ as a function of halo mass M_{vir} in Figures 10–12 for the Void, Normal, and Rarepeak volumes, respectively, at the final output redshifts of $z = (8, 12.5, 15)$. There are 468, 665, and 862 halos that have hosted metal-enriched star formation in the Void, Normal, and Rarepeak volumes, respectively, by these redshifts. From a visual inspection, the distributions from these regions look very similar, suggesting that the galaxy properties are mainly determined by their host halo masses. Most of the halos with $10^7 \lesssim M/M_{\odot} \lesssim 10^9$ have hosted metal-enriched star formation. The largest halo in the simulation suite is located in the Void region at $z = 8$ with a virial mass $M_{\text{vir}} = 5.3 \times 10^9 M_{\odot}$ and stellar mass $M_* = 1.7 \times 10^8 M_{\odot}$. There is very little star formation in halos below a virial mass of $10^7 M_{\odot}$, which is caused by a combination of a strong

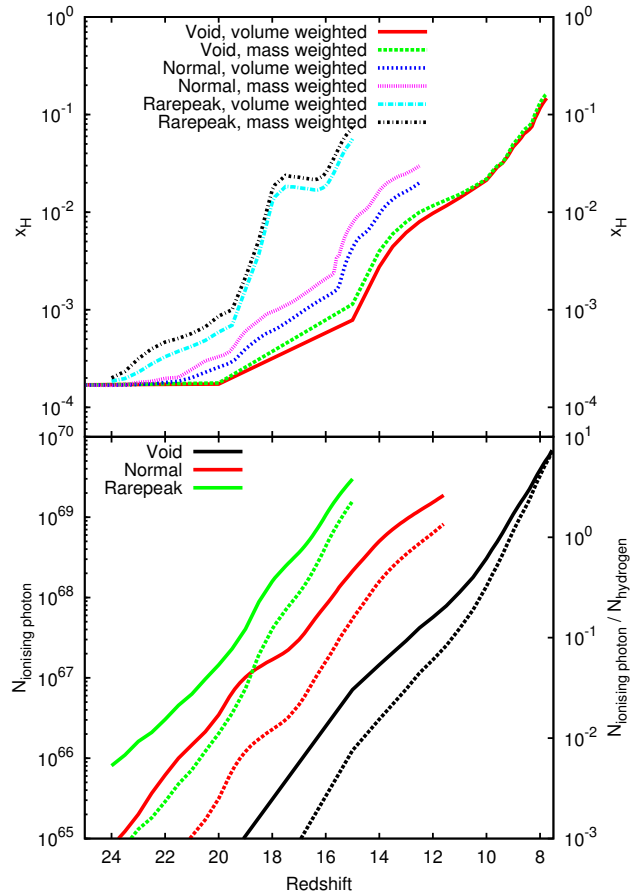


Figure 9. Top panel: volume-weighted and mass-weighted ionization fractions as a function of redshift for all simulations. Bottom panel: cumulative number of ionizing photons (solid) from all galaxies and the ratios of number of ionizing photons to number of hydrogen atoms (dotted) within the survey volumes.

UV incident radiation field, originating from nearby galaxies, and the rapid mass accretion of the halos. The UV radiation can suppress star formation in low-mass halos at all redshifts. However at earlier times, the UV radiation field is weaker, allowing for star formation to occur in such halos, but by the final redshift in the simulations most of these halos have merged into larger galaxies.

The scaling relations shown in Figures 10–12 are similar to the ones found in Wise et al. (2014), who considered the same physical processes and numerical methods as our work in a smaller (1 comoving Mpc)³ volume with a mass resolution that was 10 times smaller. We find the scatter in these relationships to be greater than in Wise et al. (2014) because our larger galaxy sample of ~ 2000 galaxies, compared to their sample of 32 galaxies, probes various large-scale environments and more importantly star formation histories, where the gas properties are greatly affected by previous stellar feedback in low-mass halos. In each of our survey volumes, the stellar mass to halo mass relation (also see Chen et al. 2014, for the Rarepeak) is consistent with the extrapolated fitting formula of Behroozi et al. (2013). The gas mass fraction varies dramatically between the extremes of nearly zero to the cosmic mean fraction in halos with $M_{\text{vir}} = 10^7 - 10^8 M_{\odot}$. These low-mass halos are heavily affected by internal and external stellar feedback, cycling between star-forming and quiescence phases (cf. Wise et al. 2012a, 2014; Hopkins et al. 2014), and

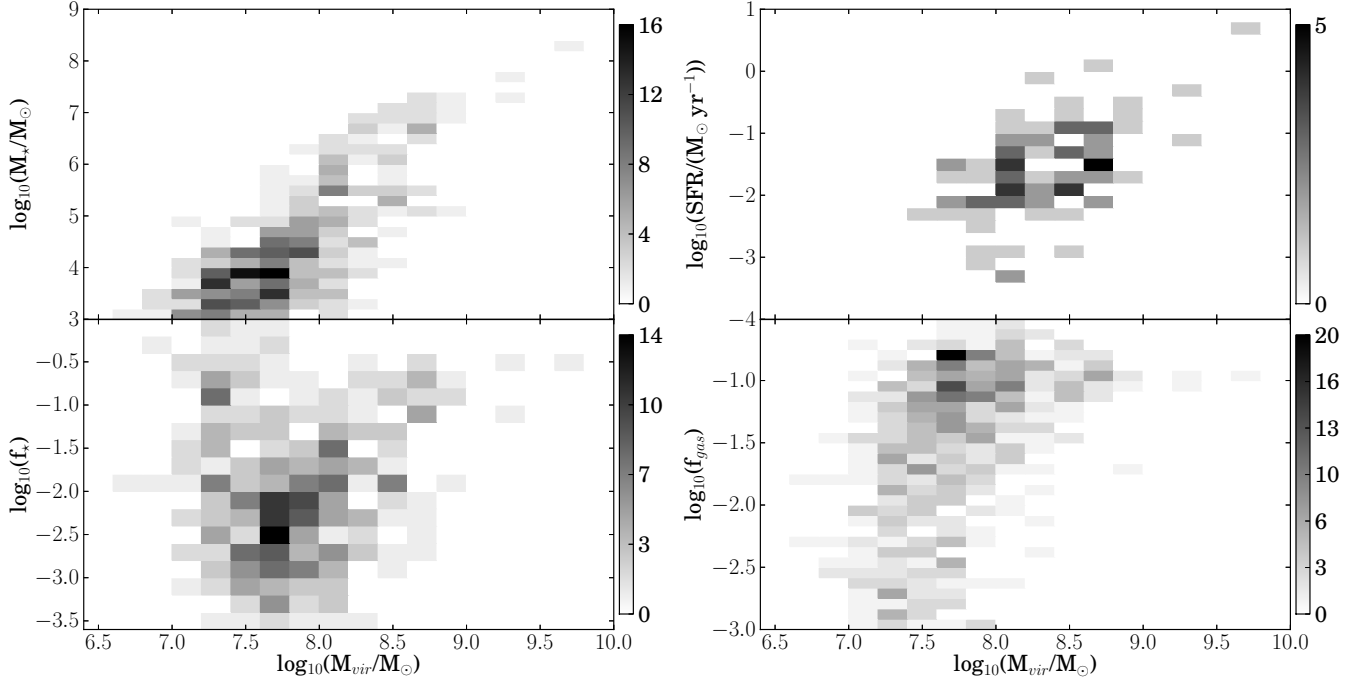


Figure 10. Distributions of (clockwise from the upper left) stellar mass, star formation rate, gas mass fraction and stellar baryonic fraction versus virial mass of all star-forming halos in the Void region at $z=8$. The pixels show the number of galaxies in the corresponding bins.

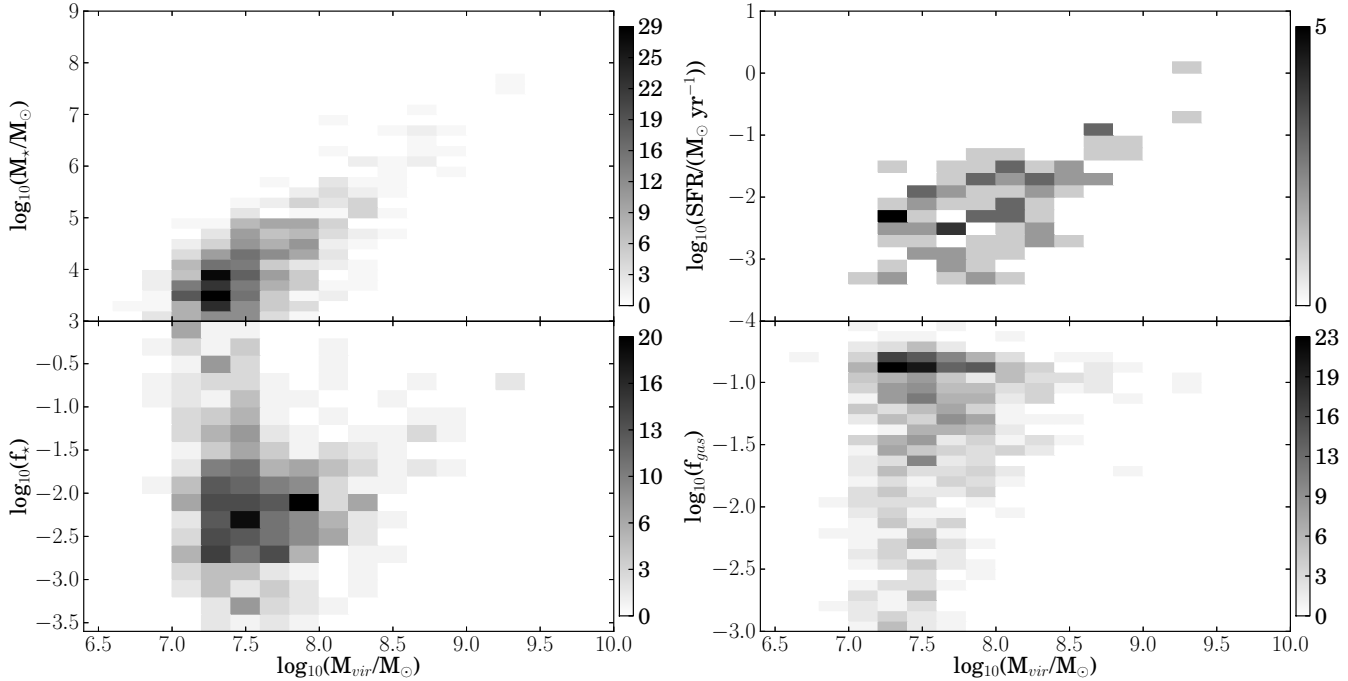


Figure 11. Same as Figure 10, but for the normal region at $z=12.5$.

their merger histories (Chen et al. 2014). For larger halos ($M_{\text{vir}} \geq 10^9 M_{\odot}$), the scatter in the scaling relations is interestingly smaller even though there are only 3–5 halos in this mass range in each region, suggesting that galaxies are less susceptible to feedback than low-mass halos and evolve on tighter scaling relations. Their gas fractions (f_{gas}) are ~ 0.1 , and their stellar baryonic fractions (f_*) lie within the approximate range 0.03–0.1. Although we only have a sample of 12 star-forming halos at these masses, we find that their proper-

ties primarily depend on their host halo masses and are less dependent on their formation histories and the environment.

It is worthwhile to compare how f_{gas} in low-mass halos depends on the environment to the assumptions made in some semi-analytical studies. For example, Dayal et al. (2014), in estimating the galaxy luminosity function (LF) from halo merger trees, assumes that $f_{\text{gas}} = 0$ after any star formation activity in halos in the mass range $10^8 - 10^9 M_{\odot}$. This assumption is only qualitatively consistent with our findings of

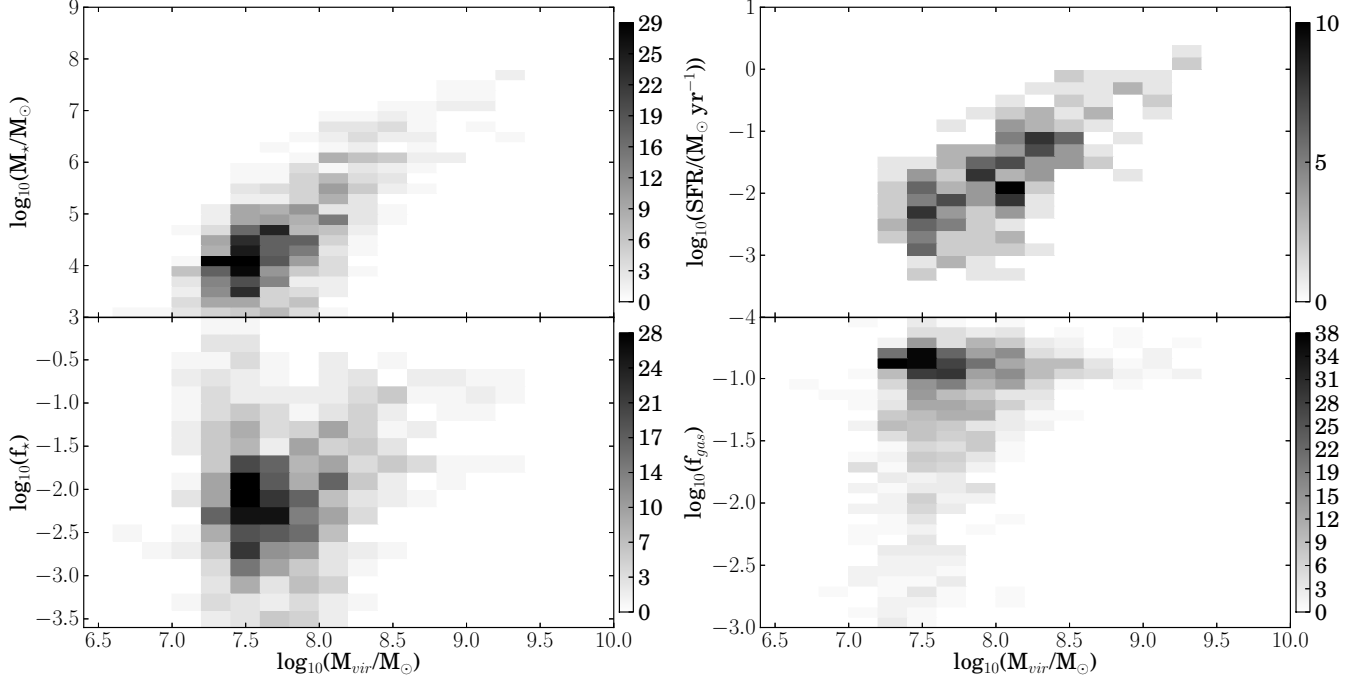


Figure 12. Same as Figure 10, but for the Rarepeak at $z = 15$.

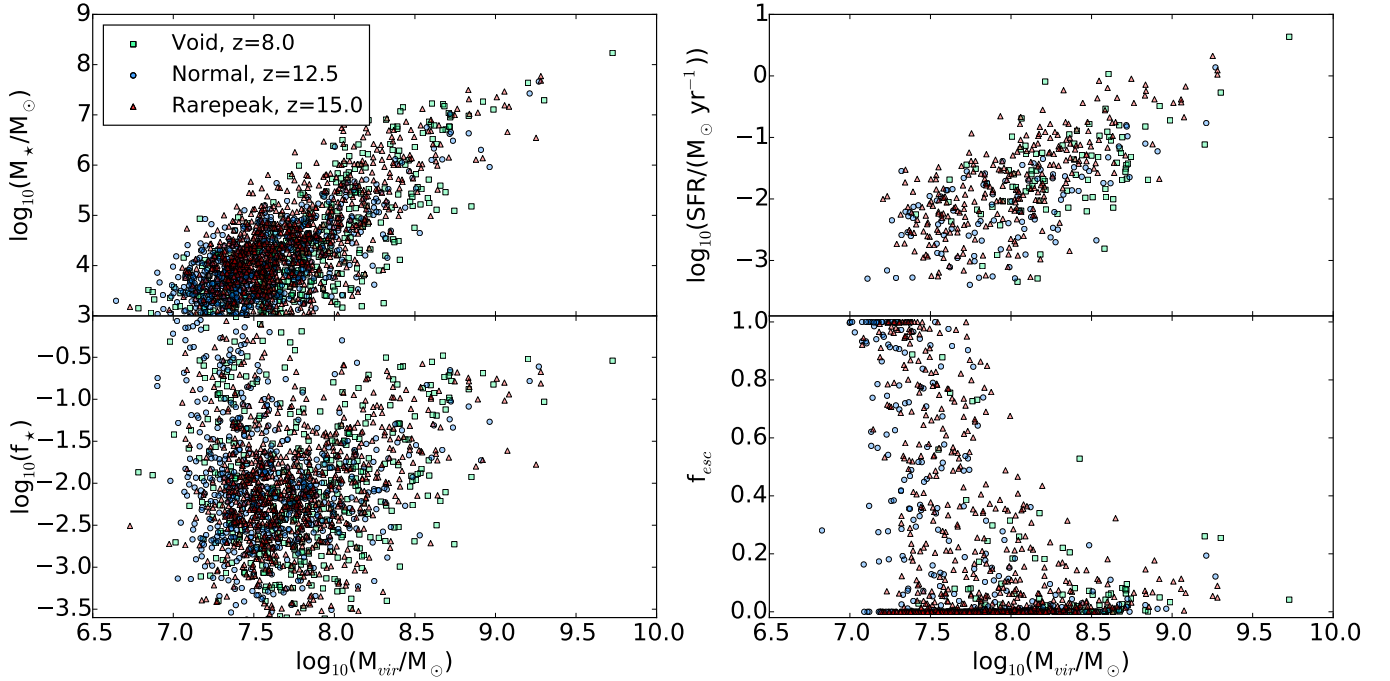


Figure 13. Distributions of (clockwise from the upper left) stellar mass, star formation rate, UV escape fraction, and stellar baryonic fraction versus virial mass of all star-forming haloes in all three simulations, Void region at $z = 8$ (green square), Normal region at $z = 12.5$ (blue circle) and Rarepeak at $z = 15$ (red triangle). Each point represents a galaxy.

the gas fraction being diminished in minihalos through radiative and supernova feedback; however, the majority of them have gas fractions above 0.05. The results from such studies may be affected when updating the models to include episodic star formation in these smallest star-forming halos.

The galaxy LF is an important quantification of the overall galaxy population, especially when calculating the intrinsic galactic ionizing emissivity. Combined with the fraction of ionizing UV radiation that escapes from the halo, the LF

faint-end slope and the behavior at very low luminosities determine the photons available for cosmic reionization. The aforementioned scaling relations or the UV galaxy LF can be used in semi-analytic reionization calculations (e.g. [Robertson et al. 2010, 2013, 2015](#); [Alvarez et al. 2012](#); [Kuhlen & Faucher-Giguère 2012](#)) to check whether galaxies can provide a sufficient amount of radiation to complete and sustain reionization by $z \sim 6$. We have presented the evolution of galaxy LFs of the Renaissance Simulations in [O’Shea et al.](#)

(2015). Summarizing the findings from that paper, there are only a few galaxies with $M_{\text{UV}} < -17$ in our survey volumes, the limiting magnitude of the HUDF at $z = 7-8$. Our simulated number densities are consistent with the LFs found in the HUDF. The simulated Renaissance Simulation LFs follow a power-law with a slope consistent with the HUDF extrapolated to low luminosities until they flatten at low luminosities of $M_{\text{UV}} \gtrsim -12$. This behavior is also seen in the higher resolution simulations of Wise et al. (2014).

3.4. Similarities of galaxies in various environments and redshifts

We have shown that the general trends and scatter of various bulk properties—UV luminosity, mass-to-light ratio, stellar masses, star formation rates, stellar baryonic fractions, and gas fractions—during the epoch of reionization are similar in each of the three survey volumes. The lack of environmental variation suggests that galaxies during their initial formation are mainly dependent on their host halo mass, and they are nearly independent of environment or redshift, given that $z \gtrsim 8$.

We now directly compare the stellar mass, stellar baryonic fraction, star formation rate, and escape fraction (see §4) as a function of halo mass from each region in Figure 13 at their final redshifts. For a more quantitative comparison, we also tabulate the galaxy properties and escape fractions (see §4) in 0.5 dex bins of M_{vir} in Table 2. Although the galaxy number densities and star formation densities vary greatly between the three survey volumes, we see that the distribution of individual galaxy properties are indistinguishable between large-scale environments with their means and variations consistent with a single population. This invariance suggests that environment and formation time play a lesser role during the formation of the first galaxies. In principle, these effects can suppress or induce star formation through preheating, enrichment, and/or halo temperatures (Gnedin 2000). However, we have found that the host halo mass is the predominant factor in controlling galaxy formation during the epoch of reionization. By comparing our simulated galaxy properties in the Void, Normal, and Rarepeak regions, we validate the method of Wise et al. (2014) and Chen et al. (2014) to use galaxies from various redshifts in a single simulation as a single sample to statistically study galaxy properties and scaling relations. We caution, however, that this technique almost certainly breaks down at later times when most halos are exposed to an external UV background, photoevaporating the low-mass halos at the end and after the epoch of reionization.

4. UV ESCAPE FRACTION AND PHOTON BUDGET

For radiation sources in galaxies to contribute to cosmic reionization, their photons must propagate into the nearby IGM, of which only a fraction f_{esc} manage to escape. The remaining fraction are absorbed by neutral gas within the virial radius of the galaxy. In order to semi-analytically calculate the evolution of the ionized fraction, the ionizing photon emissivity is required. The rate of escaping ionizing photons in a single halo can be parameterized as

$$\dot{n}_{\gamma, \text{halo}} = \psi_{\gamma} f_{\text{esc}} f_{\star} f_{\text{gas}} (\dot{M}_{\text{vir}} / \mu m_{\text{H}}) \quad (7)$$

where the product $f_{\star} f_{\text{gas}} \dot{M}_{\text{vir}}$ is the halo's instantaneous SFR, μ is the mean molecular weight, and ψ_{γ} is the number of ionizing photons produced per stellar baryon during a stellar lifetime, which can range from 6,000 for a Salpeter IMF with

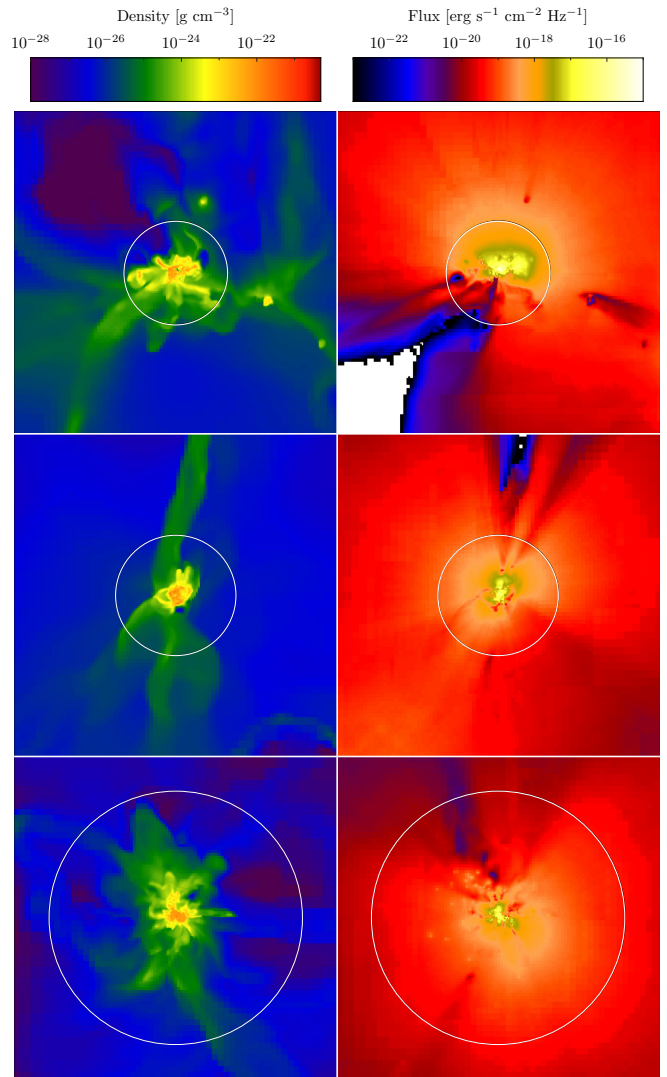


Figure 14. Projections of density-weighted average baryon density (left) and UV ($E = 21.6$ eV) flux (right) of the most massive halo in Void, Normal, and Rarepeak simulations at $z = 8, 12.5$ and 15 , respectively. These projections show the gaseous structure in the galaxy and the propagation of the UV photons. The projections have a field of view of 15 proper kpc and a depth of 600 proper pc. The white circles show the virial radii.

solar metallicity to 13,000 for a metal-poor ($[Z/H] = -3.3$) population star (Schaerer 2003). The escape fraction f_{esc} is the most uncertain factor in determining the photon budget in reionization models and has attracted much attention of numerical studies (e.g. Gnedin et al. 2008; Wise & Cen 2009; Razoumov & Sommer-Larsen 2010; Yajima et al. 2011; Paardekooper et al. 2013; Ferrara & Loeb 2013; Kimm & Cen 2014; Wise et al. 2014; Ma et al. 2015).

The UV escape fraction is notoriously difficult to calculate because it depends on the current star formation rate and density and ionization structure of the ISM, which can change rapidly from stellar feedback. Both UV radiation and SN explosions can create channels of diffuse ionized gas, spanning from star formation regions to the IGM, through which ionizing photons can escape. In other sight lines, however, there may be high density clumps or filaments that can absorb a significant fraction of ionizing radiation. Thus, the escape fraction of each galaxy can vary in the temporal, spatial, and angular domains. Our simulations include radiation transport

Table 2
Galaxy and host halo properties

$\log M_{\text{vir}} [M_{\odot}]$ (1)	Region (2)	$\log \text{SFR} [M_{\odot} \text{ yr}^{-1}]$ (3)	$\log f_{\star}$ (4)	f_{gas} (5)	$\log M_{\star} [M_{\odot}]$ (6)	f_{esc} (7)
6.75	Void	–	$-0.07^{+0.98}_{-1.80}$	$0.005^{+0.004}_{-0.004}$	$3.26^{+0.22}_{-0.20}$	–
	Normal	–	$0.24^{+1.24}_{-1.04}$	$0.008^{+0.007}_{-0.008}$	$3.44^{+0.33}_{-0.35}$	$0.64^{+0.24}_{-0.24}$
	Rarepeak	–	$-2.62^{+0.07}_{-0.07}$	$0.055^{+0.030}_{-0.030}$	$3.15^{+0.02}_{-0.02}$	–
7.25	Void	–	$-1.26^{+1.56}_{-1.39}$	$0.016^{+0.017}_{-0.016}$	$3.56^{+0.49}_{-0.46}$	$0.58^{+0.42}_{-0.57}$
	Normal	$-2.49^{+0.38}_{-0.74}$	$-1.51^{+1.94}_{-1.33}$	$0.043^{+0.081}_{-0.043}$	$3.56^{+0.58}_{-0.51}$	$0.51^{+0.49}_{-0.51}$
	Rarepeak	$-2.36^{+0.39}_{-0.38}$	$-1.97^{+1.31}_{-1.68}$	$0.069^{+0.076}_{-0.069}$	$3.67^{+0.71}_{-0.81}$	$0.42^{+0.55}_{-0.42}$
7.75	Void	$-2.09^{+0.53}_{-0.32}$	$-2.23^{+0.77}_{-0.80}$	$0.058^{+0.072}_{-0.057}$	$4.02^{+0.61}_{-0.63}$	$0.12^{+0.18}_{-0.12}$
	Normal	$-2.39^{+0.62}_{-0.58}$	$-2.17^{+0.52}_{-0.59}$	$0.071^{+0.072}_{-0.064}$	$4.14^{+0.71}_{-0.75}$	$0.17^{+0.31}_{-0.17}$
	Rarepeak	$-2.11^{+0.57}_{-0.65}$	$-2.34^{+0.68}_{-0.68}$	$0.091^{+0.065}_{-0.071}$	$4.20^{+0.74}_{-0.72}$	$0.21^{+0.35}_{-0.21}$
8.25	Void	$-1.65^{+0.53}_{-0.53}$	$-2.02^{+0.73}_{-0.82}$	$0.102^{+0.035}_{-0.029}$	$5.11^{+1.10}_{-1.20}$	$0.04^{+0.02}_{-0.04}$
	Normal	$-2.03^{+0.50}_{-0.46}$	$-1.99^{+0.46}_{-0.53}$	$0.086^{+0.046}_{-0.056}$	$5.03^{+0.63}_{-0.74}$	$0.03^{+0.01}_{-0.03}$
	Rarepeak	$-1.53^{+0.57}_{-0.59}$	$-1.85^{+0.68}_{-0.60}$	$0.118^{+0.048}_{-0.053}$	$5.38^{+0.78}_{-0.78}$	$0.07^{+0.09}_{-0.07}$
8.75	Void	$-1.33^{+0.51}_{-0.58}$	$-1.33^{+0.60}_{-0.66}$	$0.104^{+0.035}_{-0.029}$	$6.32^{+0.74}_{-0.99}$	$0.03^{+0.04}_{-0.03}$
	Normal	$-1.38^{+0.47}_{-0.36}$	$-1.38^{+0.37}_{-0.32}$	$0.095^{+0.038}_{-0.042}$	$6.24^{+0.42}_{-0.32}$	$0.02^{+0.02}_{-0.02}$
	Rarepeak	$-0.80^{+0.57}_{-0.63}$	$-1.34^{+0.56}_{-0.38}$	$0.133^{+0.021}_{-0.024}$	$6.44^{+0.61}_{-0.45}$	$0.07^{+0.05}_{-0.06}$
9.25	Void	$-0.69^{+0.29}_{-0.29}$	$-0.78^{+0.17}_{-0.17}$	$0.097^{+0.005}_{-0.005}$	$7.46^{+0.12}_{-0.12}$	$0.26^{+0.00}_{-0.00}$
	Normal	$-0.31^{+0.31}_{-0.31}$	$-0.70^{+0.06}_{-0.06}$	$0.100^{+0.001}_{-0.001}$	$7.54^{+0.81}_{-0.81}$	$0.16^{+0.02}_{-0.02}$
	Rarepeak	$-0.21^{+0.29}_{-0.23}$	$-1.05^{+0.28}_{-0.50}$	$0.141^{+0.021}_{-0.024}$	$7.23^{+0.43}_{-0.51}$	$0.07^{+0.03}_{-0.02}$

Notes: Statistics are shown for galaxies of Void region at $z = 8$, Normal region at $z = 12.5$ and Rarepeak at $z = 15$ in 0.5 dex bins in M_{vir} . Column (1): Center of mass bin. Column (2): Simulations. Column (3): Star formation rate density. Dashes indicate no recent star formation. Column (4): Stellar baryonic fraction. Column (5): Gas fraction. Column (6): Stellar mass. Column (7): Fraction of hydrogen ionizing radiation that escape the virial radius. Errors shown are 1- σ deviations.

and SNe feedback and can be used to calculate the UV escape fraction accurately in post-processing. Figure 14 shows the projections of the baryon density and UV flux of the most massive halos in the Void, Normal, and Rarepeak regions at $z = (8, 12.5, 15)$, respectively. These most massive galaxies in the Void ($M_{\text{vir}} = 5.3 \times 10^9 M_{\odot}$; $M_{\star} = 1.7 \times 10^8 M_{\odot}$), Normal ($M_{\text{vir}} = 2.7 \times 10^9 M_{\odot}$; $M_{\star} = 5.7 \times 10^7 M_{\odot}$), and Rarepeak ($M_{\text{vir}} = 1.9 \times 10^9 M_{\odot}$; $M_{\star} = 4.8 \times 10^7 M_{\odot}$) regions have escape fractions of about 0.042, 0.122 and 0.090, respectively. It is apparent that the escaping radiation is anisotropic, propagating through low-density channels in the porous ISM (Clarke & Oey 2002) and being absorbed by nearby dense gaseous clumps.

4.1. Method

Because the Renaissance Simulations transports ionizing radiation that is coupled to the energy and chemistry solver, the ionization fractions stored in the datasets are accurate. Thus, we can calculate the escape fraction of all galaxies in a post-processing analysis. We only consider absorption by neutral hydrogen, which is the dominant absorber in the energy range 10–50 eV, and neglect any other absorbing species in the following analysis. We use the same method as Wise et al. (2014) to calculate f_{esc} . We briefly describe the method next, leaving the details to the original paper.

The escape fraction of ionizing photons from a star particle to an IGM component is dependent only on the opti-

cal depth $\tau = N_{\text{HI}}(\vec{r})\sigma(E)$, where \vec{r} is the vector connecting the two points. Therefore, we can simply calculate the H I column density N_{HI} along various lines of sight and use the photo-ionization cross-section σ at $E = 21.6$ eV, which is the average photon energy of the ionizing radiation considered in our simulations. We calculate 768 lines of sight from each star particle to a sphere with radius r_{vir} , centered on the halo center and pixelated with HEALPix at level 3 (Górski et al. 2005). We then compute the associated optical depths and average $\exp(-\tau)$ over all angles to calculate $f_{i,\text{esc}}$ of a single star particle. The total UV escape fraction of a single galaxy is the luminosity-weighted average of the escape fraction $f_{i,\text{esc}}$ of all star particles in the halo.

4.2. Dependence on halo mass

Figures 15–17 show the distributions of f_{esc} and the total number of photons that escape into the IGM for individual halos in the Void, Normal, and Rarepeak regions at different redshifts, respectively. These distributions only include halos that have formed stars in the past 20 Myr – in other words, the massive stars that produce nearly all of the ionizing photons which have not yet ended their lives in supernovae. First, we focus on the f_{esc} distributions in the left panels of the Figures. Their general trends do not vary significantly with environment or redshift and follow the same behavior as the results of Wise et al. (2014). The low-mass halos with $M_{\text{vir}} \lesssim 10^8 M_{\odot}$ have a large scatter in f_{esc} that is caused by the large variations in f_{\star} and f_{gas} from halo to halo. Halos with low gas

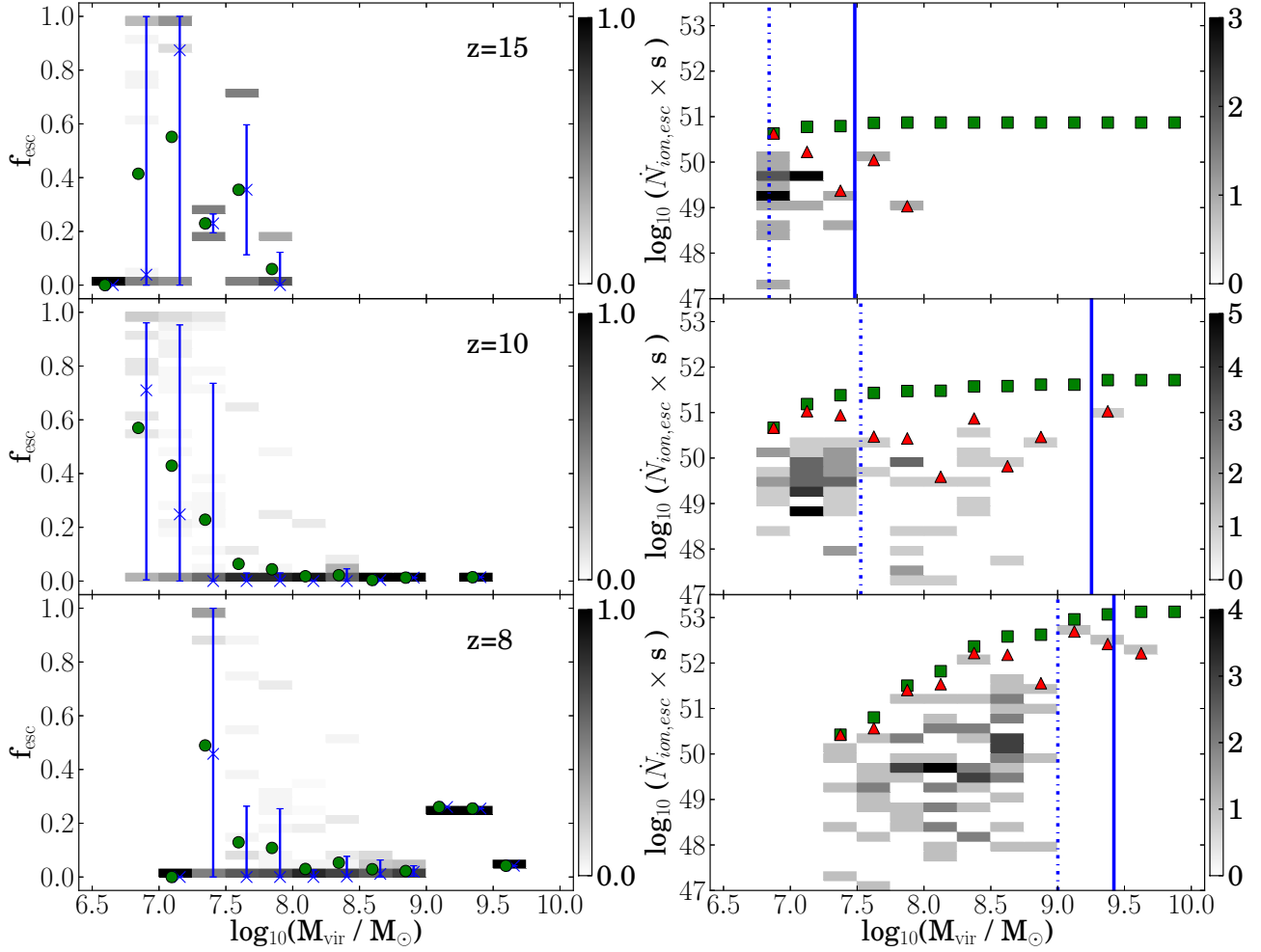


Figure 15. Probability density functions for the UV escape fraction f_{esc} (left) and number of escaped UV photons (right) as a function of halo virial mass at $z = 15$ (top), 10 (middle) and 8 (bottom) for Void region simulation. The mean escape fractions in 0.25 dex bins are represented by green filled circles. The median escape fractions are represented by blue crosses, and 15.9 and 84.1 percentiles are shown as the bottom and top of vertical lines. The number of escaped UV photons from galaxies and the cumulative number of escaped UV photons in 0.25 dex bins are represented by red triangles and green squares, respectively. The vertical dash-dotted and solid lines show the mass bins at which the cumulative UV escaped photons are half and 90% of the total escaped photons, respectively.

fractions and/or high stellar baryonic fractions have the highest f_{esc} values. The smallest halos hosting metal-enriched star formation with $M_{\text{vir}} \simeq 10^7 M_{\odot}$ have a median f_{esc} between 0.4 and 0.6, regardless of redshift and region. The median of the escape fraction steadily decreases with increasing halo mass until it reaches ~ 0.05 in the range $M_{\text{vir}} = 10^8 - 10^9 M_{\odot}$. However, it should be noted that our most massive galaxies ($M_{\text{vir}} > 10^9 M_{\odot}$) in each region have their f_{esc} values boosted to 0.1–0.2 as they experience strong continuous star formation with $\text{SFR} \sim 1 M_{\odot} \text{ yr}^{-1}$ and $\text{sSFR} \sim 10^{-8} \text{ yr}^{-1}$.

The right panels of Figures 15–17 show the distributions of the number of UV photons that escape into the IGM from each halo as a function of halo mass. We also show the total number of escaping photons (red triangles) in each mass bin, along with the cumulative number of escaping photons (green squares) below a given halo mass in the panels. To clearly denote which halos are producing most of the escaping UV photons, we mark the halo mass in which 50% (dash-dotted lines) and 90% (solid lines) of the ionizing photons are produced in halos below these marked masses. At early times before any $10^9 M_{\odot}$ halos form, the majority of the escaped

photons originate in halos below the atomic cooling threshold ($M_{\text{vir}} \simeq 10^8 M_{\odot}$). However once more massive halos form at later times, they contribute about half of the escaping UV photons to the photon budget, even though our simulations only capture the formation of a few halos with $M_{\text{vir}} > 10^9 M_{\odot}$ in each region.

4.3. Dependence on recent star formation

We have shown that the escape fraction depends on the halo mass, but in principle it should also depend on the strength and timing of the star formation because of the growth and breakout of H II regions from young stellar populations. Previous groups (Wise & Cen 2009; Wise et al. 2014; Kimm & Cen 2014) have found a correlation between the SFR and f_{esc} with some delay as the ionization front propagates beyond the virial radius. Figure 18 plots the f_{esc} distribution as a function of the stellar baryonic fraction f_{\star} (left panels) and the stellar mass fraction in young stars (right panels), or equivalently the sSFR, for all three regions at their final redshifts. To calculate the sSFR, we use the SFR averaged over the past 20 Myr. We find no general trends in f_{esc} with either quantity and also observe a large scatter in f_{esc} in both. However, there

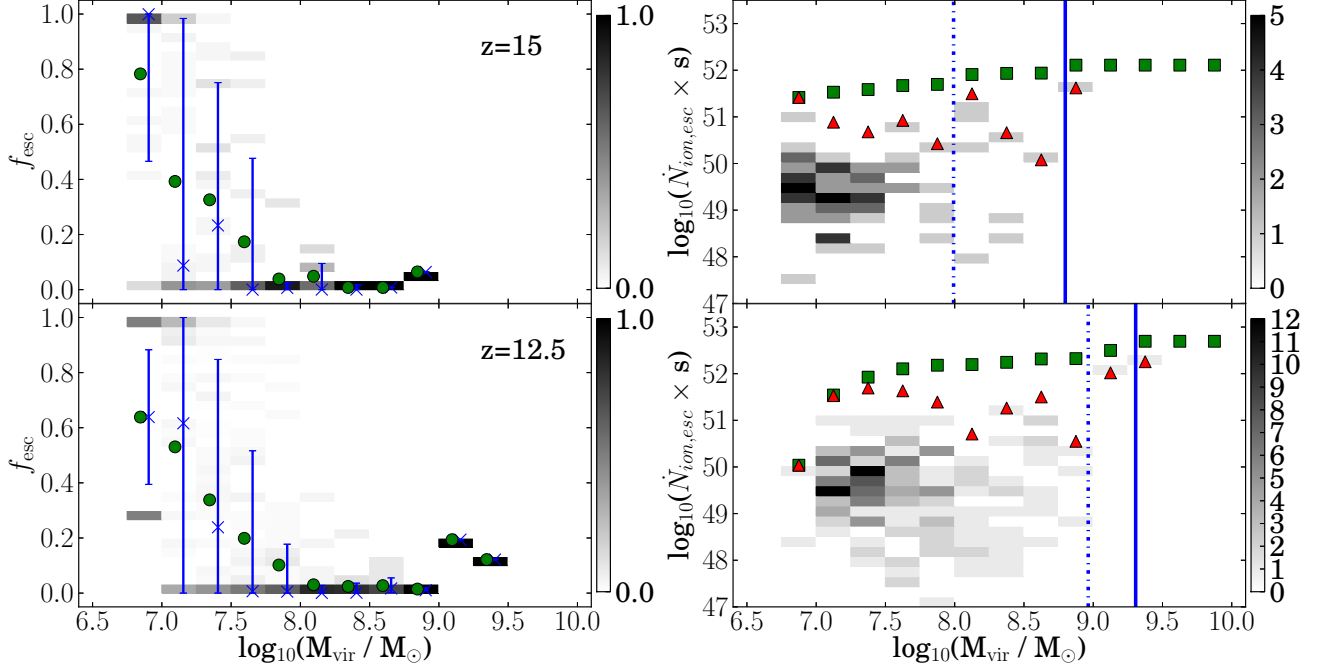


Figure 16. Same as Figure 15, but for the normal region at $z = 15$ and 12.5 .

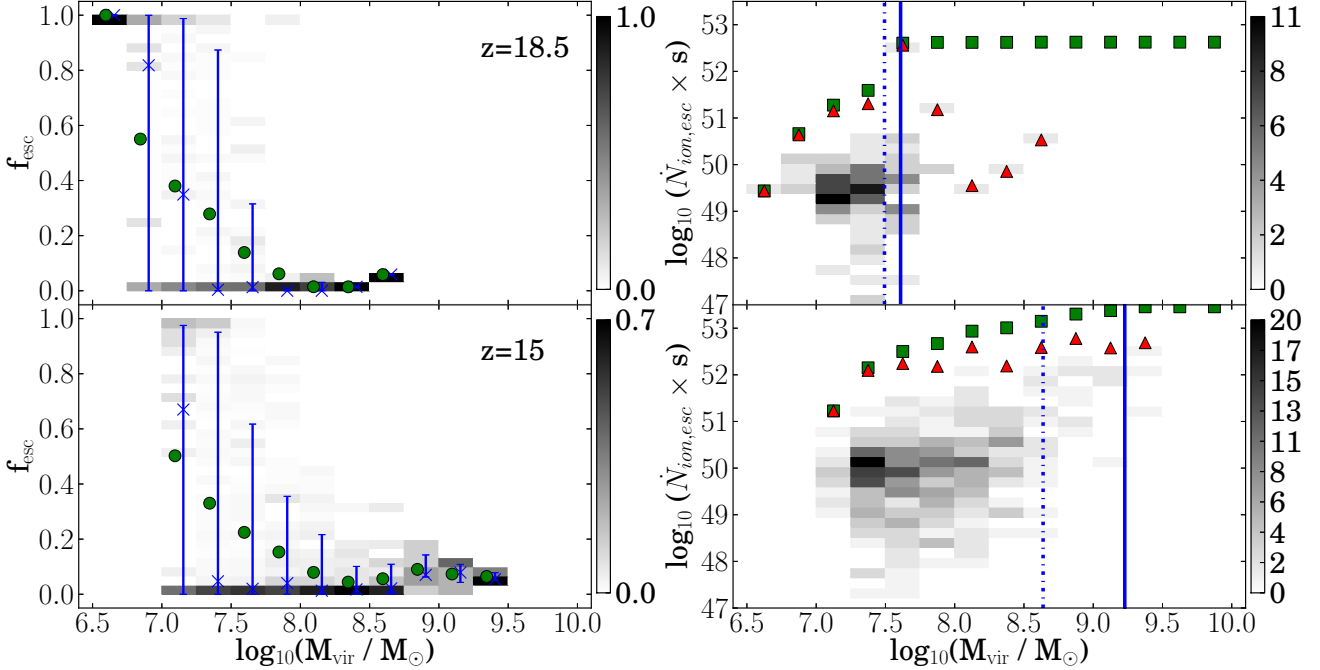


Figure 17. Same as Figure 15, but for the Rarepeak at $z = 18.5$ and 15 .

is an indication of an upward trend at $f_{\star} \gtrsim 0.1$. This scenario is rare and occurs when the halo is partially photo-evaporated, leaving behind a dense core and diffuse envelope. Once stars form in this core, the ionization front breaks out of the birth cloud and is largely unimpeded by the photo-evaporated envelope. This behavior also manifests itself in the highest sSFR bin with several halos having $f_{\text{esc}} \gtrsim 0.5$. With the exception of this extreme behavior at large f_{\star} values, the UV escape fractions are largely independent of these star formation measures and vary substantially between halos in our simulated sample

of ~ 2000 galaxies.

4.4. Fractions of halos with star formation and photons escaped

Gas in low mass halos are easily disrupted and expelled from the shallow potential wells as the outflows generated by ionization fronts and SNe easily exceed the escape velocity. This feedback diminishes the available fuel for star formation. After some time elapses, the cold gas reservoir is replenished by either cosmological infall or any gas remaining in the halo

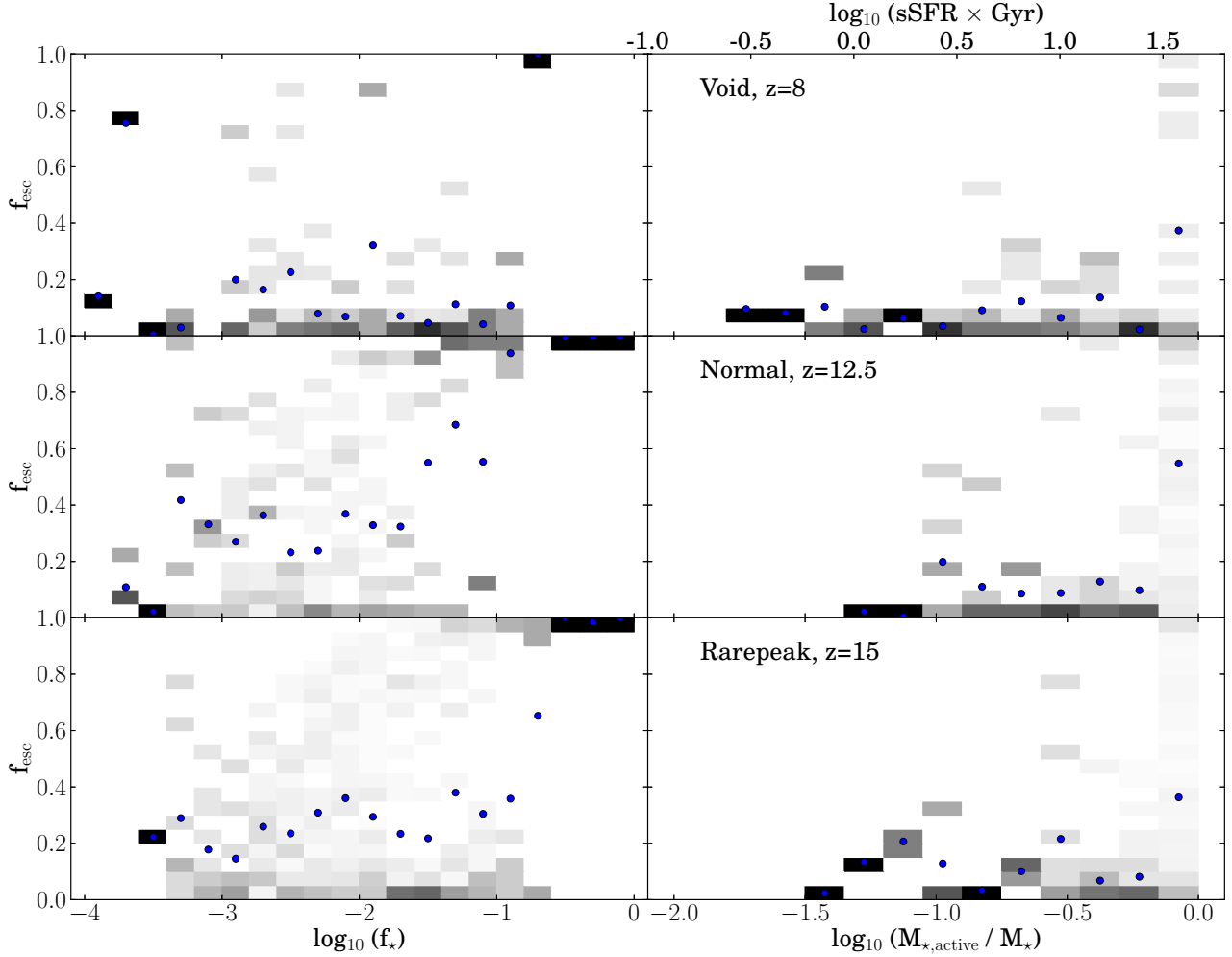


Figure 18. The UV escape fraction as a function of stellar baryonic fraction f_* (left) and ratio of young (< 20 Myr) UV radiative active stellar mass (right) of three simulations at $z = 8, 12.5,$ and $15,$ respectively. The top axis of the right panel shows the corresponding specific star formation rate (sSFR) using the average SFR for the past 20 Myr. The blue circles show the average UV escape fraction.

cooling after the massive stars have died. This cycle results in highly stochastic star formation in the lower-mass halos in our simulations. Figure 19 quantifies this behavior by plotting the fraction of halos with active star formation (left panel), i.e., stars younger than 20 Myr, and the fraction of halos with a non-zero f_{esc} (right panel) as a function of halo mass. We show these fractions for all three regions at various redshifts. Only 10% of the $M_{\text{vir}} \sim 10^7 M_{\odot}$ halos are hosting recent star formation at the times shown, regardless of the redshift and region. This fraction then increases with halo mass to $\sim 50\%$ by $M_{\text{vir}} \sim 10^8 M_{\odot}$, culminating in all halos with $M_{\text{vir}} \geq 10^9 M_{\odot}$ hosting recent star formation. These galaxy occupation fractions increase similarly with halo mass in all regions at the times shown. However for a given region, this fraction decreases as time progresses at $M_{\text{vir}} \lesssim 10^8 M_{\odot}$ because of the increasing effects of radiative feedback from more massive galaxies, effectively increasing the filtering halo mass for efficient cooling and thus star formation (cf. Gnedin 2000; Wise & Abel 2008a). Lastly because ionizing radiation originates from massive stars, the fraction of halos generating escaping photons, shown in the right panel of Figure 19, follow a similar trend as the stellar occupation fraction.

5. CONCLUSIONS

In this paper, we have quantified the properties and the UV escape fraction of galaxies during the epoch of reionization, expanding upon the work of Wise et al. (2014) with a much larger sample of $\sim 2,000$ galaxies and extending the relations to a maximum halo mass of $\sim 10^{9.5} M_{\odot}$. To establish these relations, we have run and analyzed the *Renaissance Simulations*, a suite of high-resolution radiation hydrodynamics simulations of the first galaxies in three different large-scale environments, each with a comoving volume of $\sim 200 \text{ Mpc}^3$, that follow Pop III star formation and the transition to metal-enriched stars in thousands of halos.

In particular, we have analyzed these halos to determine any trends in star formation and gas fraction with halo mass and environment. Using our large sample of first galaxies, we showed that their characteristic properties and contribution to the photon budget of reionization are mainly determined by their halo masses and are nearly independent of the environment and redshift during the epoch of reionization. This finding validates the assumption of Wise et al. (2014) and Chen et al. (2014) that the galaxy population during this epoch is nearly invariant with redshift, which allowed them to increase their effective galaxy sample size by combining datasets at

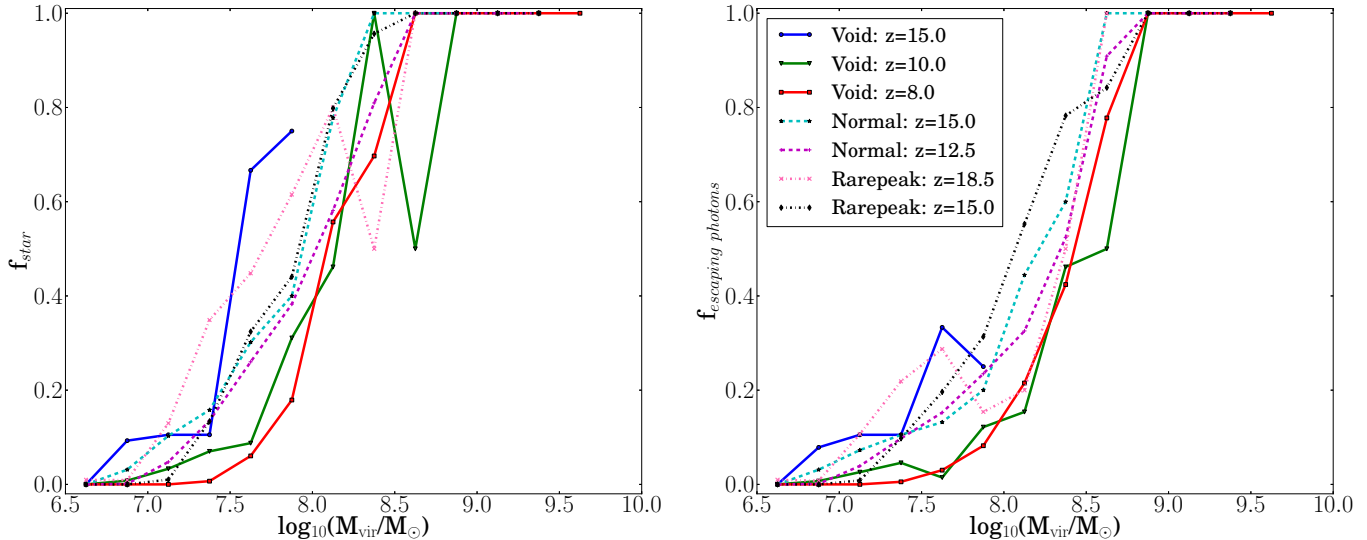


Figure 19. Fractions of halos with active star formation (stars younger than 20 Myr) (left) and photons escaped from their virial radius (right) as a function of the halo mass.

different redshifts into a single sample.

We found that galaxies with $M_{\text{vir}} < 10^9 M_{\odot}$ are consistent with the high-resolution simulation results of [Wise et al. \(2014\)](#), which only followed the formation of 32 galaxies by $z \sim 7$. This result is not unexpected because we use the same star formation and feedback models; however, it does show that these models give a consistent result even with a mass and spatial resolution that is a factor of 10 times larger. Given our larger volume, we are able to extend these relations to halos with masses up to $10^{9.5} M_{\odot}$. Equivalently, our simulated UV galaxy LF now extends to $M_{1500} \simeq -18$ and matches the abundances of the faintest galaxies observed at $z = 7-8$. We find that our LF follow a similar power law seen in observations (e.g. [Bouwens et al. 2015](#); [Finkelstein et al. 2015](#)), but extends to very faint galaxies with $M_{1500} \simeq -12$ and flattens above this absolute magnitude ([Wise et al. 2014](#); [O’Shea et al. 2015](#)).

These larger galaxies provide some insight into the evolution of the stellar sources of cosmic reionization. We found that the decreasing trend of f_{esc} with halo mass with a minimum of 0.05 between $10^8 - 10^9 M_{\odot}$; however the mean f_{esc} values stabilize around 0.1–0.2 at halo masses $M_{\text{vir}} \gtrsim 10^9 M_{\odot}$, which is consistent with previous findings of [Kimm & Cen \(2014\)](#). Once halos reach this mass, they are largely resistant to SN feedback and external radiative feedback (e.g. [Efstathiou 1992](#); [Thoul & Weinberg 1996](#); [Okamoto et al. 2008](#); [Finlator et al. 2011](#)). They initially host relatively strong (i.e., significant sSFR) and continuous star formation, and coupled with an escape fraction in the range 0.1–0.2, they provide a large fraction ($\sim 50\%$) of the photon budget of reionization at late times (see also [Sharma et al. 2016](#)).

We see that the faintest galaxies below the atomic cooling limit ($M_{\text{vir}} \lesssim 10^8 M_{\odot}$) dominate the photon budget during the initial stages of reionization, but then their star formation is suppressed, leaving more massive galaxies to provide the majority of UV radiation to complete reionization. However, the escape fraction alone does not tell the whole story. Although low-mass galaxies generate most of the ionizing photons at early times, the earliest low-mass galaxies tend to form in overdense regions with high recombination rates, resulting in smaller H II regions. This effect is apparent in the neutral frac-

tion projections in [Figure 8](#), where the cosmological H II regions are contained completely in the collapsing large-scale overdensity. Although these early galaxies ionize a substantial mass fraction of their local environment, they add little to the overall ionized photons needed for complete reionization at $z \sim 6-7$. We only see significant growth of the volume- and mass-weighted ionization fraction at late times – in particular in the Void region at $z = 8$. Nevertheless, these faintest galaxies play an important role in heating the surrounding IGM and shaping internal gaseous galactic properties that affect subsequent galaxy formation.

This research was supported by National Science Foundation (NSF) grant AST-1109243 to MLN. JHW acknowledges support from NSF grants AST-1211626 and AST-1333360 and Hubble theory grants HST-AR-13895 and HST-AR-14326. KA was supported by the NRF grant NRF-2014R1A1A2059811. BWO was supported in part by the sabbatical visitor program at the Michigan Institute for Research in Astrophysics (MIRA) at the University of Michigan in Ann Arbor, by NASA grants NNX12AC98G, NNX15AP39G, and by Hubble Theory Grants HST-AR-13261.01-A and HST-AR-14315.001-A. The simulation was performed using ENZO on the Blue Waters operated by the National Center for Supercomputing Applications (NCSA) with PRAC allocation support by the NSF (award number ACI-0832662). Data analysis was performed on the Gordon supercomputer operated for XSEDE by the San Diego Supercomputer Center and on the Blue Waters supercomputer. This research is part of the Blue Waters sustained-petascale computing project, which is supported by the NSF (award number ACI 1238993) and the state of Illinois. Blue Waters is a joint effort of the University of Illinois at Urbana-Champaign and its NCSA. This research has made use of NASA’s Astrophysics Data System Bibliographic Services. The majority of the analysis and plots were done with YT ([Turk et al. 2011](#)). ENZO and YT are developed by a large number of independent researchers from numerous institutions around the world. Their commitment to open science has helped make this work possible.

- Abel, T., Wise, J. H., & Bryan, G. L. 2007, *ApJ*, 659, L87
- Ahn, K., Iliev, I. T., Shapiro, P. R., Mellema, G., Koda, J., & Mao, Y. 2012, *ApJ*, 756, L16
- Ahn, K., Shapiro, P. R., Iliev, I. T., Mellema, G., & Pen, U.-L. 2009, *ApJ*, 695, 1430
- Ahn, K., Xu, H., Norman, M. L., Alvarez, M. A., & Wise, J. H. 2015, *ApJ*, 802, 8
- Alvarez, M. A., Finlator, K., & Trenti, M. 2012, *ApJ*, 759, L38
- Behroozi, P. S., Wechsler, R. H., & Conroy, C. 2013, *ApJ*, 770, 57
- Bouwens, R. J., Illingworth, G. D., Oesch, P. A., Labbé, I., Trenti, M., van Dokkum, P., Franx, M., Stiavelli, M., Carollo, C. M., Magee, D., & Gonzalez, V. 2011, *ApJ*, 737, 90
- Bouwens, R. J., Illingworth, G. D., Oesch, P. A., Trenti, M., Labbé, I., Bradley, L., Carollo, M., van Dokkum, P. G., Gonzalez, V., Holwerda, B., Franx, M., Spitler, L., Smit, R., & Magee, D. 2015, *ApJ*, 803, 34
- Bovill, M. S., & Ricotti, M. 2011, *ApJ*, 741, 18
- Boylan-Kolchin, M., Bullock, J. S., & Garrison-Kimmel, S. 2014, *MNRAS*, 443, L44
- Bromm, V., Yoshida, N., & Hernquist, L. 2003, *ApJ*, 596, L135
- Bruzual, G., & Charlot, S. 2003, *MNRAS*, 344, 1000
- Bryan, G. L., Norman, M. L., O'Shea, B. W., Abel, T., Wise, J. H., Turk, M. J., Reynolds, D. R., Collins, D. C., Wang, P., Skillman, S. W., Smith, B., Harkness, R. P., Bordner, J., Kim, J.-h., Kuhlen, M., Xu, H., Goldbaum, N., Hummels, C., Kritsuk, A. G., Tasker, E., Skory, S., Simpson, C. M., Hahn, O., Oishi, J. S., So, G. C., Zhao, F., Cen, R., Li, Y., & The Enzo Collaboration. 2014, *ApJS*, 211, 19
- Bullock, J. S., Kravtsov, A. V., & Weinberg, D. H. 2000, *ApJ*, 539, 517
- Chen, P., Wise, J. H., Norman, M. L., Xu, H., & O'Shea, B. W. 2014, *ApJ*, 795, 144
- Clarke, C., & Oey, M. S. 2002, *MNRAS*, 337, 1299
- Coe, D., Zitrin, A., Carrasco, M., Shu, X., Zheng, W., Postman, M., Bradley, L., Koekemoer, A., Bouwens, R. G., Broadhurst, T., Monna, A., Host, O., Moustakas, L. A., Ford, H., Moustakas, J., van der Wel, A., Donahue, M., Rodney, S. A., Benítez, N., Jouvel, S., Seitz, S., Kelson, D. D., & Rosati, P. 2013, *ApJ*, 762, 32
- Conroy, C., & Kratter, K. M. 2012, *ApJ*, 755, 123
- Cooke, J., Ryan-Weber, E. V., Garel, T., & Díaz, C. G. 2014, *MNRAS*, 441, 837
- Dayal, P., Ferrara, A., Dunlop, J. S., & Pacucci, F. 2014, *MNRAS*, 445, 2545
- Dove, J. B., Shull, J. M., & Ferrara, A. 2000, *ApJ*, 531, 846
- Efstathiou, G. 1992, *MNRAS*, 256, 43P
- Ellis, R. S., McLure, R. J., Dunlop, J. S., Robertson, B. E., Ono, Y., Schenker, M. A., Koekemoer, A., Bowler, R. A. A., Ouchi, M., Rogers, A. B., Curtis-Lake, E., Schneider, E., Charlot, S., Stark, D. P., Furlanetto, S. R., & Cirasuolo, M. 2013, *ApJ*, 763, L7
- Fan, X., Carilli, C. L., & Keating, B. 2006, *ARA&A*, 44, 415
- Ferrara, A., & Loeb, A. 2013, *MNRAS*, 431, 2826
- Finkelstein, S. L., Ryan, Jr., R. E., Papovich, C., Dickinson, M., Song, M., Somerville, R. S., Ferguson, H. C., Salmon, B., Giavalisco, M., Koekemoer, A. M., Ashby, M. L. N., Behroozi, P., Castellano, M., Dunlop, J. S., Faber, S. M., Fazio, G. G., Fontana, A., Groggin, N. A., Hathi, N., Jaacks, J., Kocevski, D. D., Livermore, R., McLure, R. J., Merlin, E., Mobasher, B., Newman, J. A., Rafelski, M., Tilvi, V., & Willner, S. P. 2015, *ApJ*, 810, 71
- Finlator, K., Davé, R., & Özel, F. 2011, *ApJ*, 743, 169
- Fujita, A., Martin, C. L., Mac Low, M.-M., & Abel, T. 2003, *ApJ*, 599, 50
- Gardner, J. P., Mather, J. C., Clampin, M., Doyon, R., Greenhouse, M. A., Hammel, H. B., Hutchings, J. B., Jakobsen, P., Lilly, S. J., Long, K. S., Lunine, J. I., McCaughrean, M. J., Mountain, M., Nella, J., Rieke, G. H., Rieke, M. J., Rix, H.-W., Smith, E. P., Sonneborn, G., Stiavelli, M., Stockman, H. S., Windhorst, R. A., & Wright, G. S. 2006, *Space Sci. Rev.*, 123, 485
- Gilmozzi, R., & Spyromilio, J. 2007, *The Messenger*, 127, 11
- Gnedin, N. Y. 2000, *ApJ*, 542, 535
- 2008, *ApJ*, 673, L1
- 2016, *ArXiv e-prints* (1603.07729)
- Gnedin, N. Y., & Kravtsov, A. V. 2006, *ApJ*, 645, 1054
- Gnedin, N. Y., Kravtsov, A. V., & Chen, H.-W. 2008, *ApJ*, 672, 765
- Górski, K. M., Hivon, E., Banday, A. J., Wandelt, B. D., Hansen, F. K., Reinecke, M., & Bartelmann, M. 2005, *ApJ*, 622, 759
- Grazian, A., Giallongo, E., Gerbasi, R., Fiore, F., Fontana, A., Le Fèvre, O., Pentericci, L., Vanzella, E., Zamorani, G., Cassata, P., Garilli, B., Le Brun, V., Maccagni, D., Tasca, L. A. M., Thomas, R., Zucca, E., Amorín, R., Bardelli, S., Cassarà, L. P., Castellano, M., Cimatti, A., Cucciati, O., Durkalec, A., Giavalisco, M., Hathi, N. P., Ilbert, O., Lemaux, B. C., Paltani, S., Ribeiro, B., Schaerer, D., Scoddeggio, M., Sommariva, V., Talia, M., Tresse, L., Vergani, D., Bonchi, A., Boutsia, K., Capak, P., Charlot, S., Contini, T., de la Torre, S., Dunlop, J., Fotopoulou, S., Gaia, L., Koekemoer, A., López-Sanjuan, C., Mellier, Y., Merlin, E., Paris, D., Pforr, J., Pilo, S., Santini, P., Scoville, N., Taniguchi, Y., & Wang, P. W. 2016, *A&A*, 585, A48
- Greif, T. H., Glover, S. C. O., Bromm, V., & Klessen, R. S. 2010, *ApJ*, 716, 510
- Hahn, O., & Abel, T. 2011, *MNRAS*, 415, 2101
- Hopkins, P. F., Kereš, D., Oñorbe, J., Faucher-Giguère, C.-A., Quataert, E., Murray, N., & Bullock, J. S. 2014, *MNRAS*, 445, 581
- Inoue, A. K., & Iwata, I. 2008, *MNRAS*, 387, 1681
- Jeon, M., Pawlik, A. H., Bromm, V., & Milosavljević, M. 2014, *MNRAS*, 444, 3288
- Johns, M., McCarthy, P., Raybould, K., Bouchez, A., Farahani, A., Filgueira, J., Jacoby, G., Sheckman, S., & Sheehan, M. 2012, in *Society of Photo-Optical Instrumentation Engineers (SPIE) Conference Series*, Vol. 8444, *Society of Photo-Optical Instrumentation Engineers (SPIE) Conference Series*
- Karlsson, T., Johnson, J. L., & Bromm, V. 2008, *ApJ*, 679, 6
- Kimm, T., & Cen, R. 2014, *ApJ*, 788, 121
- Kitayama, T., & Yoshida, N. 2005, *ApJ*, 630, 675
- Kitayama, T., Yoshida, N., Susa, H., & Umemura, M. 2004, *ApJ*, 613, 631
- Komatsu, E., Smith, K. M., Dunkley, J., Bennett, C. L., Gold, B., Hinshaw, G., Jarosik, N., Larson, D., Nolte, M. R., Page, L., Spergel, D. N., Halpern, M., Hill, R. S., Kogut, A., Limon, M., Meyer, S. S., Odegard, N., Tucker, G. S., Weiland, J. L., Wollack, E., & Wright, E. L. 2011, *ApJS*, 192, 18
- Kuhlen, M., & Faucher-Giguère, C.-A. 2012, *MNRAS*, 423, 862
- Ma, X., Hopkins, P. F., Kasen, D., Quataert, E., Faucher-Giguère, C.-A., Keres, D., & Murray, N. 2016, *ArXiv e-prints* (1601.07559)
- Ma, X., Kasen, D., Hopkins, P. F., Faucher-Giguère, C.-A., Quataert, E., Keres, D., & Murray, N. 2015, *MNRAS*, 453, 960
- Machacek, M. E., Bryan, G. L., & Abel, T. 2001, *ApJ*, 548, 509
- McConnachie, A. W. 2012, *AJ*, 144, 4
- McLure, R. J., Dunlop, J. S., Bowler, R. A. A., Curtis-Lake, E., Schenker, M., Ellis, R. S., Robertson, B. E., Koekemoer, A. M., Rogers, A. B., Ono, Y., Ouchi, M., Charlot, S., Wild, V., Stark, D. P., Furlanetto, S. R., Cirasuolo, M., & Targett, T. A. 2013, *MNRAS*, 432, 2696
- McLure, R. J., Dunlop, J. S., de Ravel, L., Cirasuolo, M., Ellis, R. S., Schenker, M., Robertson, B. E., Koekemoer, A. M., Stark, D. P., & Bowler, R. A. A. 2011, *MNRAS*, 418, 2074
- Muratov, A. L., Gnedin, O. Y., Gnedin, N. Y., & Zemp, M. 2013, *ApJ*, 772, 106
- Nestor, D. B., Shapley, A. E., Kornei, K. A., Steidel, C. C., & Siana, B. 2013, *ApJ*, 765, 47
- Oesch, P. A., Brammer, G., van Dokkum, P. G., Illingworth, G. D., Bouwens, R. J., Labbé, I., Franx, M., Momcheva, I., Ashby, M. L. N., Fazio, G. G., Gonzalez, V., Holden, B., Magee, D., Skelton, R. E., Smit, R., Spitler, L. R., Trenti, M., & Willner, S. P. 2016, *ApJ*, 819, 129
- Okamoto, T., Gao, L., & Theuns, T. 2008, *MNRAS*, 390, 920
- O'Shea, B. W., & Norman, M. L. 2008, *ApJ*, 673, 14
- O'Shea, B. W., Wise, J. H., Xu, H., & Norman, M. L. 2015, *ApJ*, 807, L12
- Paardekooper, J.-P., Khochfar, S., & Dalla Vecchia, C. 2013, *MNRAS*, 429, L94
- 2015, *MNRAS*, 451, 2544
- Paardekooper, J.-P., Pelupessy, F. I., Altay, G., & Kruij, C. J. H. 2011, *A&A*, 530, A87
- Planck Collaboration, Ade, P. A. R., Aghanim, N., Arnaud, M., Ashdown, M., Aumont, J., Baccigalupi, C., Banday, A. J., Barreiro, R. B., Bartlett, J. G., & et al. 2015, *ArXiv e-prints* (1502.01589)
- Press, W. H., & Schechter, P. 1974, *ApJ*, 187, 425
- Razoumov, A. O., & Sommer-Larsen, J. 2007, *ApJ*, 668, 674
- 2010, *ApJ*, 710, 1239
- Ricotti, M., & Shull, J. M. 2000, *ApJ*, 542, 548
- Robertson, B. E., Ellis, R. S., Dunlop, J. S., McLure, R. J., & Stark, D. P. 2010, *Nature*, 468, 49
- Robertson, B. E., Ellis, R. S., Furlanetto, S. R., & Dunlop, J. S. 2015, *ApJ*, 802, L19
- Robertson, B. E., Furlanetto, S. R., Schneider, E., Charlot, S., Ellis, R. S., Stark, D. P., McLure, R. J., Dunlop, J. S., Koekemoer, A., Schenker, M. A., Ouchi, M., Ono, Y., Curtis-Lake, E., Rogers, A. B., Bowler, R. A. A., & Cirasuolo, M. 2013, *ApJ*, 768, 71
- Salvadori, S., & Ferrara, A. 2009, *MNRAS*, 395, L6
- Salvadori, S., Tolstoy, E., Ferrara, A., & Zaroubi, S. 2014, *MNRAS*, 437, L26
- Schaerer, D. 2002, *A&A*, 382, 28
- 2003, *A&A*, 397, 527
- Schaye, J., Crain, R. A., Bower, R. G., Furlong, M., Schaller, M., Theuns, T., Dalla Vecchia, C., Frenk, C. S., McCarthy, I. G., Helly, J. C., Jenkins, A., Rosas-Guevara, Y. M., White, S. D. M., Baes, M., Booth, C. M., Camps, P., Navarro, J. F., Qu, Y., Rahmati, A., Sawala, T., Thomas, P. A., & Trayford, J. 2015, *MNRAS*, 446, 521
- Sharma, M., Theuns, T., Frenk, C., Bower, R., Crain, R., Schaller, M., & Schaye, J. 2016, *MNRAS*, 458, L94
- Sheth, R. K., & Tormen, G. 1999, *MNRAS*, 308, 119
- Siana, B., Shapley, A. E., Kulas, K. R., Nestor, D. B., Steidel, C. C., Teplitz, H. I., Alavi, A., Brown, T. M., Conselice, C. J., Ferguson, H. C., Dickinson, M., Giavalisco, M., Colbert, J. W., Bridge, C. R., Gardner, J. P., & de Mello, D. F. 2015, *ApJ*, 804, 17
- Simard, L. 2013, *Journal of Astrophysics and Astronomy*, 34, 97
- Thou, A. A., & Weinberg, D. H. 1996, *ApJ*, 465, 608
- Truelove, J. K., Klein, R. L., McKee, C. F., Holliman, II, J. H., Howell, L. H., Greenough, J. A., & Woods, D. T. 1998, *ApJ*, 495, 821
- Turk, M. J., Smith, B. D., Oishi, J. S., Skory, S., Skillman, S. W., Abel, T., & Norman, M. L. 2011, *ApJS*, 192, 9

- Vanzella, E., Guo, Y., Giavalisco, M., Grazian, A., Castellano, M., Cristiani, S., Dickinson, M., Fontana, A., Nonino, M., Giallongo, E., Pentericci, L., Galametz, A., Faber, S. M., Ferguson, H. C., Grogin, N. A., Koekemoer, A. M., Newman, J., & Siana, B. D. 2012, *ApJ*, 751, 70
- Warren, M. S., Abazajian, K., Holz, D. E., & Teodoro, L. 2006, *ApJ*, 646, 881
- Weisz, D. R., Johnson, B. D., & Conroy, C. 2014, *ApJ*, 794, L3
- Whalen, D., Abel, T., & Norman, M. L. 2004, *ApJ*, 610, 14
- Whalen, D., van Veelen, B., O’Shea, B. W., & Norman, M. L. 2008, *ApJ*, 682, 49
- Wheeler, C., Oñorbe, J., Bullock, J. S., Boylan-Kolchin, M., Elbert, O. D., Garrison-Kimmel, S., Hopkins, P. F., & Kereš, D. 2015, *MNRAS*, 453, 1305
- Wise, J. H., & Abel, T. 2005, *ApJ*, 629, 615
- 2007, *ApJ*, 671, 1559
- 2008a, *ApJ*, 684, 1
- 2008b, *ApJ*, 685, 40
- 2011, *MNRAS*, 414, 3458
- Wise, J. H., Abel, T., Turk, M. J., Norman, M. L., & Smith, B. D. 2012a, *MNRAS*, 427, 311
- Wise, J. H., & Cen, R. 2009, *ApJ*, 693, 984
- Wise, J. H., Demchenko, V. G., Halicek, M. T., Norman, M. L., Turk, M. J., Abel, T., & Smith, B. D. 2014, *MNRAS*, 442, 2560
- Wise, J. H., Turk, M. J., Norman, M. L., & Abel, T. 2012b, *ApJ*, 745, 50
- Wood, K., & Loeb, A. 2000, *ApJ*, 545, 86
- Xu, H., Ahn, K., Wise, J. H., Norman, M. L., & O’Shea, B. W. 2014, *ApJ*, 791, 110
- Xu, H., Norman, M. L., O’Shea, B. W., & Wise, J. H. 2016, *ArXiv e-prints* (1604.03586)
- Xu, H., Wise, J. H., & Norman, M. L. 2013, *ApJ*, 773, 83
- Yajima, H., Choi, J.-H., & Nagamine, K. 2011, *MNRAS*, 412, 411
- Zheng, W., Postman, M., Zitrin, A., Moustakas, J., Shu, X., Jouvel, S., Høst, O., Molino, A., Bradley, L., Coe, D., Moustakas, L. A., Carrasco, M., Ford, H., Benítez, N., Lauer, T. R., Seitz, S., Bouwens, R., Koekemoer, A., Medezinski, E., Bartelmann, M., Broadhurst, T., Donahue, M., Grillo, C., Infante, L., Jha, S. W., Kelson, D. D., Lahav, O., Lemze, D., Melchior, P., Meneghetti, M., Merten, J., Nonino, M., Ogaz, S., Rosati, P., Umetsu, K., & van der Wel, A. 2012, *Nature*, 489, 406